Cell Metabolism

Article

Adipocyte-derived ferroptotic signaling mitigates obesity

Graphical abstract

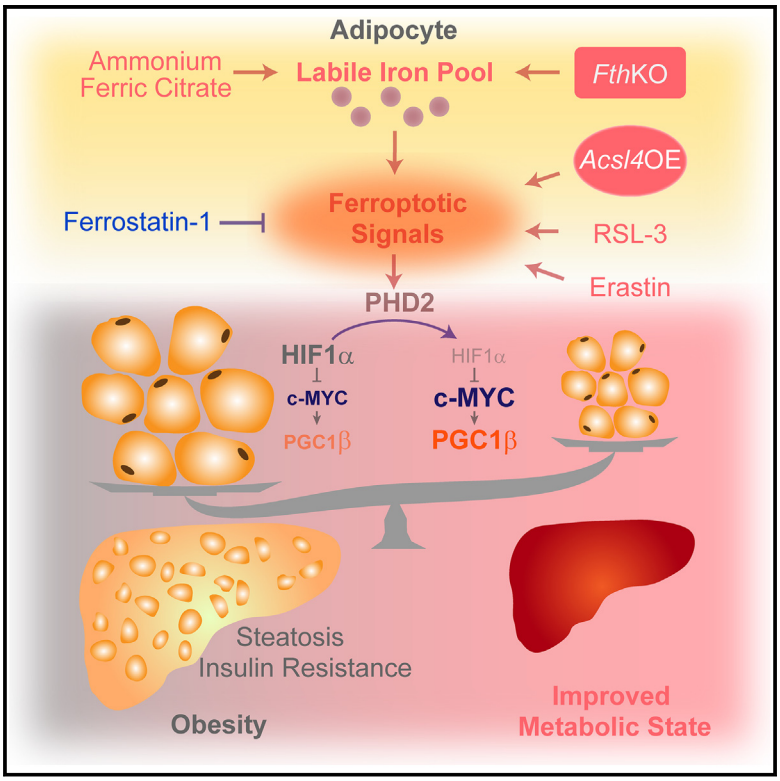

Highlights

- A ferroptotic signature is lower in adipose tissues in humans with obesity
- Adipose *Acsl4* overexpression or *Fth* deletion mitigates obesity by ferroptotic signaling
- Ferroptotic signaling in adipocytes reduces lipid deposits by a HIF1α-c-MYC-PGC1β axis
- 5,15-DiHETE induces ferroptotic signaling in adipocytes to enhance thermogenesis

Authors

Xue Wang, Qian Wu, Meijuan Zhong, ..., Wanting Shi, Junxia Min, Fudi Wang

Correspondence

junxiamin@zju.edu.cn (J.M.), fwang@zju.edu.cn (F.W.)

In brief

Wang et al. show that a ferroptosis signature is compromised in adipose tissues of humans and mice with obesity. By constraining HIF1α availability, ferroptotic signaling in adipocytes reduces lipid accumulation and increases thermogenesis via a c-Myc-Pgc1β axis, and thus, targeting this pathway may prevent or treat obesity and metabolic disorders.

Wang et al., 2025, Cell Metabolism *37*, 1–19
March 4, 2025
https://doi.org/10.1016/j.cmet.2024.11.010

CellPress

Cell Metabolism

CellPress
OPEN ACCESS

Article

Adipocyte-derived ferroptotic signaling mitigates obesity

Xue Wang,[1,2,3,4,7] Qian Wu,[5,7] Meijuan Zhong,[3] Ying Chen,[6] Yudi Wang,[2] Xin Li,[3] Wenxi Zhao,[1] Chaodong Ge,[2] Xinhui Wang,[1] Yingying Yu,[2] Sisi Yang,[1] Tianyi Wang,[3] Enjun Xie,[1] Wanting Shi,[1] Junxia Min,[2,*] and Fudi Wang[1,3,4,8,*]

[1]The Second Affiliated Hospital, School of Public Health, State Key Laboratory of Experimental Hematology, Zhejiang University School of Medicine, Hangzhou 310058, China
[2]The First Affiliated Hospital, Institute of Translational Medicine, Zhejiang University School of Medicine, Hangzhou 310058, China
[3]School of Public Health, Basic Medical Sciences, School of Pharmacology, The First Affiliated Hospital, Hengyang Medical School, University of South China, Hengyang 421001, China
[4]School of Public Health, School of Basic Medical Sciences, Xinxiang Medical University, Xinxiang 453003, China
[5]International Institutes of Medicine, The Fourth Affiliated Hospital of Zhejiang University School of Medicine, Yiwu, Zhejiang, China
[6]Ministry of Education Key Laboratory of Metabolism and Molecular Medicine, Department of Endocrinology and Metabolism, Zhongshan Hospital, Fudan University, Shanghai, China
[7]These authors contributed equally
[8]Lead contact
*Correspondence: junxiamin@zju.edu.cn (J.M.), fwang@zju.edu.cn (F.W.)
https://doi.org/10.1016/j.cmet.2024.11.010

SUMMARY

Ferroptosis is characterized as an iron-dependent and lipophilic form of cell death. However, it remains unclear what role ferroptosis has in adipose tissue function and activity. Here, we find a lower ferroptotic signature in the adipose tissue of individuals and mice with obesity. We further find that activation of ferroptotic signaling by a non-lethal dose of ferroptosis agonists significantly reduces lipid accumulation in primary adipocytes and high-fat diet (HFD)-fed mice. Notably, adipocyte-specific overexpression of acyl-coenzyme A synthetase long-chain family member 4 (*Acsl4*) or deletion of ferritin heavy chain (*Fth*) protects mice from HFD-induced adipose expansion and metabolic disorders via activation of ferroptotic signaling. Mechanistically, we find that 5,15-dihydroxyeicosatetraenoic acid (5,15-DiHETE) activates ferroptotic signaling, resulting in the degradation of hypoxia-inducible factor-1α (HIF1α), thereby derepressing a thermogenic program regulated by the c-Myc-peroxisome proliferator-activated receptor gamma coactivator-1 beta (Pgc1β) pathway. Our findings suggest that activating ferroptosis signaling in adipose tissues might help to prevent and treat obesity and its related metabolic disorders.

INTRODUCTION

Obesity is a global epidemic and is characterized by a chronic state of excess energy storage over energy utilization. Adipose tissue stores excess nutrients during obesity, reconfiguring systemic metabolism and elevating the risk of metabolic disorders.[1] Thus, gaining a better understanding of adipose homeostasis will aid in the development of new strategies for managing obesity.

Ferroptosis, a form of cell death that relies on iron-dependent lipid peroxidation of membrane lipids, has been implicated in a wide range of diseases.[2–7] For ferroptosis to occur, specific membrane lipids containing polyunsaturated fatty acids (PUFAs) must undergo oxidation, and natural mechanisms for scavenging oxidized lipids must be compromised.[8] Acyl-coenzyme A synthetase long-chain family member 4 (ACSL4) is an important ferroptosis facilitator as it incorporates free PUFAs into membranes to promote their peroxidation.[8] By contrast, glutathione (GSH) peroxidase 4 (GPX4) works as a core ferroptosis suppressor as it utilizes reduced GSH to eliminate phospholipid hydroperoxide, through which GSH is oxidized into glutathione disulfide (GSSG).[8]

One piece of evidence supporting the role of ferroptosis in adipose homeostasis is the effect of ferroptosis agonists in lipid-related studies. For example, iron supplementation, which can induce ferroptosis, activates fatty acid β-oxidation and increases mitochondrial function, ultimately reducing fat mass in mice[9–11]; however, whether ferroptosis occurs in this process has not been studied.[9,11] Conversely, blocking iron uptake specifically in the adipose tissue by depleting transferrin receptor 1 dampens thermogenesis in the brown adipose tissue (BAT).[12] In addition, the core ferroptosis suppressor GPX4 is essential in the differentiation of adipocytes,[13] suggesting an increasing demand for reducing lipid peroxidation during *in vitro* adipocyte differentiation. However, knocking out *Gpx4* in adipocytes only moderately affects adipose homeostasis,[13] suggesting the existence of alternative and/or redundant pathways apart from

Please cite this article in press as: Wang et al., Adipocyte-derived ferroptotic signaling mitigates obesity, Cell Metabolism (2024), https://doi.org/10.1016/j.cmet.2024.11.010

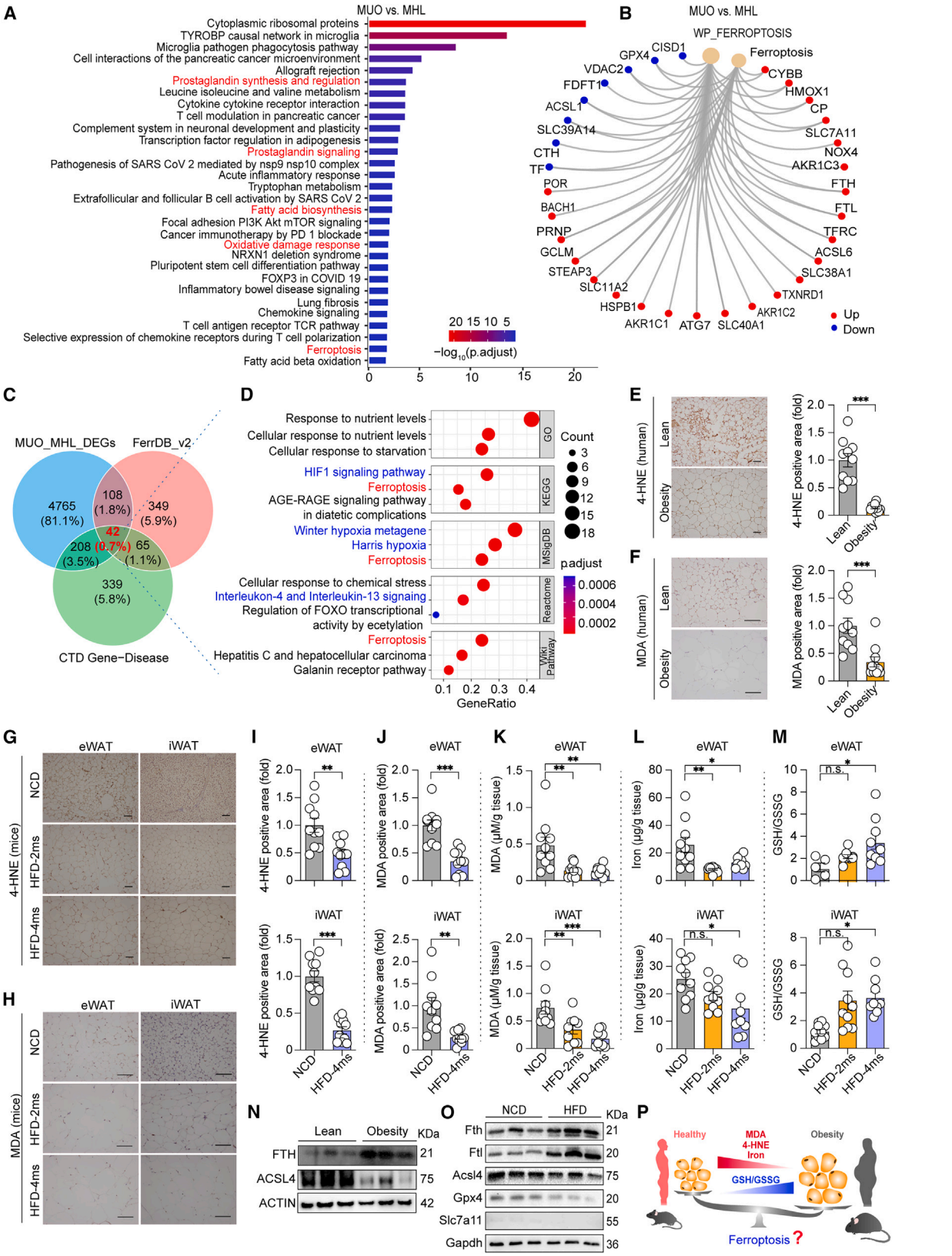

(legend on next page)

Please cite this article in press as: Wang et al., Adipocyte-derived ferroptotic signaling mitigates obesity, Cell Metabolism (2024), https://doi.org/10.1016/j.cmet.2024.11.010

Gpx4. These pathways may include the ferroptosis suppressor protein 1 (FSP1)-coenzyme Q10 (CoQ10)-NAD(P)H axis[14] or the canonical iron sequester system comprised of ferritin heavy chain (FTH) and ferritin light chain (FTL).[15,16] Nevertheless, whether these pathways are physiologically relevant in the adipose tissue remains an open question.

Here, we show that ferroptotic signaling elicited by ferroptosis agonists reduces fat accumulation in primary adipocytes and in high-fat diet (HFD)-fed mice. Moreover, we found that both ACSL4 and FTH regulate ferroptotic signaling and adipose expansion in HFD-fed mice. This role of ferroptotic signaling is due to its ability to upregulate prolyl hydroxylase domain 2 (Phd2) and thus destabilize hypoxia-inducible factor-1α (HIF1α) protein levels, thereby enhancing a thermogenic program regulated by a c-Myc-peroxisome proliferator-activated receptor gamma coactivator-1 beta (Pgc1β) pathway. Together, these findings suggest that targeting ferroptotic signaling in adipocytes may serve as a potential strategy to mitigate obesity.

RESULTS

An adipose tissue ferroptosis pathway is associated with obesity

To understand whether ferroptosis in adipocytes plays a role in human obesity and metabolic disorders, we first interrogated a publicly available RNA sequencing dataset.[17] We found that the ferroptosis pathway and gene clusters that regulate ferroptosis/ferroptosis sensitivity, including prostaglandin synthesis and regulation,[18,19] fatty acid biosynthesis,[20,21] and oxidative damage response,[22,23] were differentially expressed in subcutaneous abdominal adipose tissue obtained from individuals with metabolically unhealthy obesity (MUO) compared with those obtained from individuals who are metabolically healthy and lean (MHL) (Figure 1A). For example, canonical anti-ferroptotic genes, such as *SLC7A11* (encoding the cystine-glutamate antiporter xCT), *FTH*, and *FTL* were higher, whereas *GPX4* was lower, in the MUO group compared with the MHL group (Figure 1B). However, we found that the canonical pro-ferroptotic gene *ACSL4* did not show any difference between the groups, while *ACSL1* was lower and *ACSL6* was higher in the MUO group vs. the MHL group (Figure 1B). To further predict the interactive component of ferroptosis in obesity, we extracted the overlapped genes between the differentially expressed genes in MUO vs. MHL with a ferroptosis gene database (FerrDB) and with CTD Gene Disease (The Comparative Toxicogenomics Database). Briefly, we identified 42 genes (Table S1) as obesity/disease-related ferroptotic genes (Figure 1C). Notably, these genes were significantly enriched in pathways, including response to nutrients/starvation/stress, interleukin-4 (IL-4) and IL-13 signaling, as well as HIF1α signaling pathway/hypoxia (Figure 1D), suggesting that stress responses either from nutrition/oxygen restriction or inflammation closely collaborate with the ferroptosis pathway during obesity.

Having established a link between the ferroptosis pathway in obesity and potential interacting mediators (i.e., inflammation, hypoxia, etc.), we then confirmed the occurrence of ferroptosis in adipose tissue from humans with obesity and in a mouse model of obesity (diet-induced obesity) by measuring markers of lipid peroxidation. The latter is characterized by the accumulation of a series of complex aldehydes derived from lipid peroxides (LOOHs), among which malondialdehyde (MDA) and 4-hydroxynonenal (4-HNE) are the most abundant and often used as markers of ferroptosis.[24–26] We found that compared with lean controls, individuals with obesity had significantly lower levels of lipid peroxidation byproducts 4-HNE (Figure 1E) and MDA (Figure 1F) in the abdominal adipose tissue. Similarly, compared with mice fed a normal chow diet (NCD), HFD-fed mice had significantly lower levels of 4-HNE and MDA (Figures 1G–1J) staining in the epididymal white adipose tissue (eWAT), inguinal white adipose tissue (iWAT), and BAT (Figures S1A–S1D). Meanwhile, the MDA content and non-heme iron content in the eWAT (Figures 1K and 1L), iWAT (Figures 1K and 1L), and BAT (Figure S1E) were lower in HFD-fed mice vs. NCD-fed mice. Conversely, the GSH/oxidized GSH (GSH/GSSG) ratio in the eWAT and the iWAT (Figure 1M), but not the BAT (Figure S1E), were higher in HFD mice vs. NCD mice. In line with previous studies,[27] we observed greater hepatic 4-HNE and MDA staining (Figures S1A–S1D), as well as higher MDA content and non-heme iron content (Figure S1F), with no difference in the GSH/GSSG ratio (Figure S1F), in the liver of HFD-fed mice compared with NCD-fed mice. These ferroptosis signatures did not significantly change in the gastrocnemius muscle from HFD-fed mice compared with NCD-fed mice (Figures S1A, S1B, and S1G). These data depict a diversified pattern of ferroptosis signature in metabolic tissues (adipose tissue, liver, and muscle) under an HFD challenge, where in particular, the ferroptosis signature is less pronounced in the adipose tissue in individuals and mice with obesity.

Figure 1. Adipose ferroptosis signature is weakened in obesity

(A) Functional annotation of the differentially expressed genes (DEGs) in MUO compared with MHL, utilizing the Wiki database.

(B) Genes enriched in the ferroptosis pathway from Kyoto Encyclopedia of Genes and Genomes (KEGG) and The Molecular Signatures Database (MsigDB) databases.

(C) Venn diagram illustrating the overlap of genes among MUO and MHL DEGs, curated gene set associated with obesity from CTD database, and FerrDB gene set.

(D) Functionally enriched terms for the intersected genes, based on Gene Ontology-Biological Process (GO-BP), KEGG database, MsigDB, Reactome, and WikiPathways.

(E–J) Images and quantification of 4-HNE or MDA staining from abdominal adipose samples in individuals with obesity vs. lean condition (E and F) from eWAT and iWAT in mice 2 or 4 months after consuming an HFD or NCD (G–J). Scale bars, 100 μm.

(K–M) MDA, non-heme iron content, and GSH/GSSG ratio, measured in eWAT and iWAT obtained from HFD-fed and NCD-fed mice (n = 5–10).

(N) Western blot analysis of FTH, ACSL4, and ACTIN proteins in abdominal adipose lysates obtained from individuals with obesity vs. lean condition (n = 3).

(O) Western blot analysis of the indicated protein in eWAT obtained from mice 4 months after feeding an HFD or NCD (n = 3).

(P) A diagram illustrating the changes in the adipose ferroptosis signature in obesity.

Data are presented as mean ± SEM. n.s., not significant; *p < 0.05; **p < 0.01; ***p < 0.001 (one-way ANOVA or unpaired Student's t test).

Please cite this article in press as: Wang et al., Adipocyte-derived ferroptotic signaling mitigates obesity, Cell Metabolism (2024), https://doi.org/10.1016/j.cmet.2024.11.010

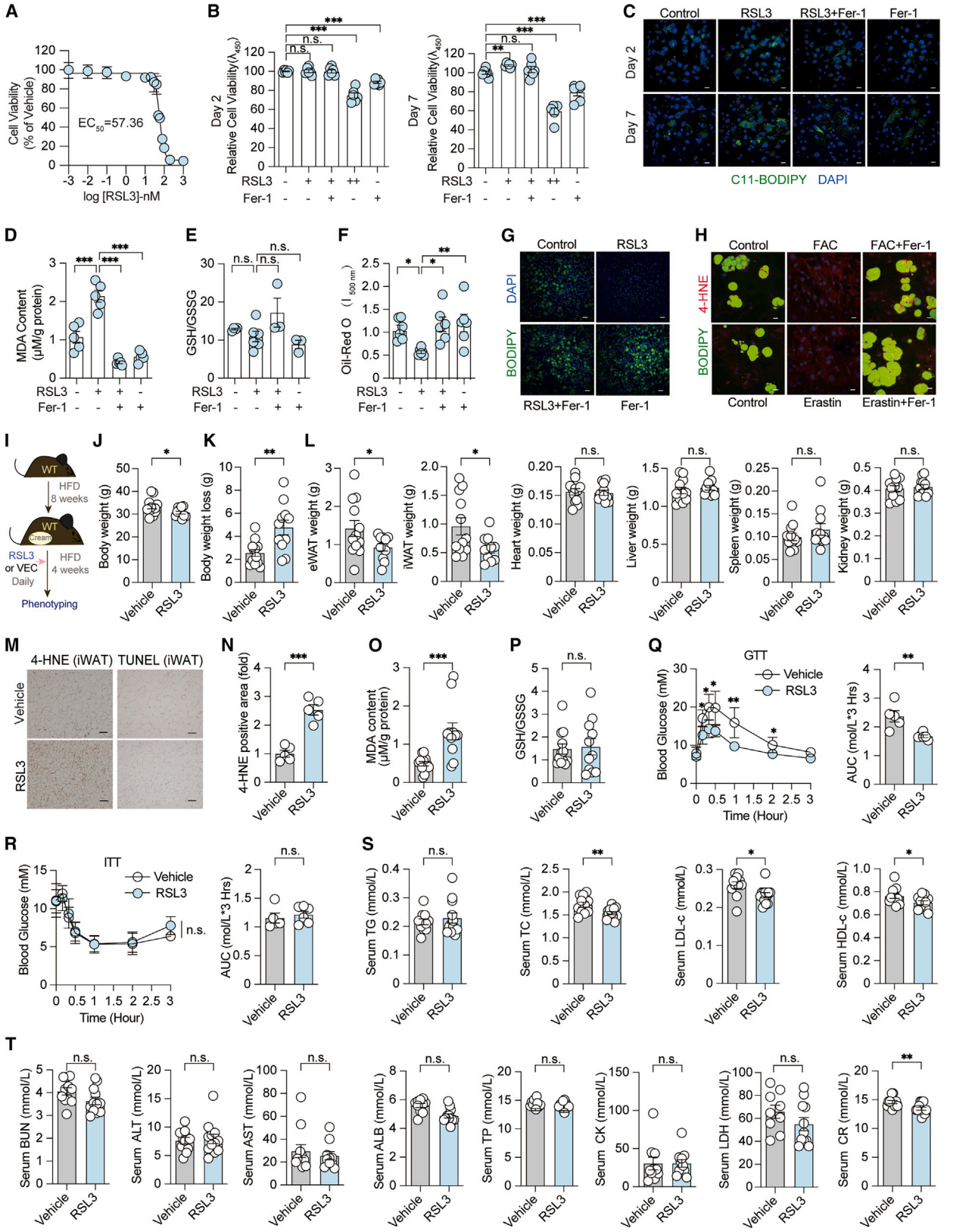

(legend on next page)

Please cite this article in press as: Wang et al., Adipocyte-derived ferroptotic signaling mitigates obesity, Cell Metabolism (2024), https://doi.org/10.1016/j.cmet.2024.11.010

In support of these observations, we found that protein levels of FTH were higher, while the protein levels of ACSL4 were lower, in abdominal adipose tissue from individuals with obesity vs. those who were lean (Figures 1N and S1H). Similarly, Fth and Ftl protein levels were higher (Figures 1O and S1I), while Gpx4, Slc7a11, and Acsl4 protein levels were significantly lower in the eWAT of HFD-fed mice compared with NCD-fed mice (Figures 1O and S1I). Together, these findings suggest that the ferroptosis pathway in the adipose tissue is inversely correlated with obesity and that it may participate in the development of obesity (Figure 1P).

Ferroptotic signaling reduces fat accumulation

To interrogate whether the ferroptosis pathway can regulate adipose tissue homeostasis, we conducted *in vitro* experiments using the stromal vascular fraction (SVF) isolated from the white adipose tissue of C57BL/6 mice. The SVFs were cultured in adipose differentiation medium in the presence or absence of the ferroptosis agonists RAS-selective lethal 3 (RSL3), erastin, or ammonium ferric citrate (FAC). We monitored adipocyte maturation for 7 days.

We first asked whether adipocytes are sensitive to RSL3 exposure by performing a cell viability assay. Of note, compared with other cell types,[28,29] we found that the SVFs were highly susceptible to RSL3-induced ferroptosis (half-maximal inhibitory concentration [IC_{50}] = 57.36 nM, Figure 2A). Next, we tested the effect of a non-lethal dose of RSL3 (30 nM) on adipocyte differentiation (Figures 2B and 2C). We observed higher levels of lipid reactive oxygen species (ROS) in RSL3-treated SVFs in both the early (day 2) and final stages of adipocyte differentiation (day 7) compared with control-treated SVFs, as indicated by increased C11-BODIPY mean fluorescence intensity (Figure 2C) and higher levels of MDA (Figure 2D). Moreover, the ferroptosis inhibitor ferrostatin-1 (Fer-1) prevented the RSL3-induced elevation in lipid ROS (Figure 2C) and MDA (Figure 2D). RSL3 treatment did not change the ratio of GSH/GSSG in the SVFs (Figure 2E), likely due to reduced consumption of GSH via Gpx4.[30,31] These data indicate that a non-lethal dose of RSL3 leads to a clear induction of a ferroptosis feature (lipid peroxidation) without causing cell death (as suggested by the results of the cell viability assay). We therefore refer to this treatment as a trigger of *ferroptotic signaling* rather than as ferroptosis per se, as the latter is a form of cell death.

Notably, we found that ferroptotic signaling elicited by the non-lethal dose of RSL3 (hereafter simply referred to as RSL3 treatment) resulted in a lower content of lipid droplets in SVFs compared with control-treated SVFs on day 7, as indicated by oil red O (Figure 2F) and BODIPY 493/503 staining of neutral lipids (Figure 2G). In addition, both FAC and erastin treatment resulted in greater lipid peroxidation and a lower content of lipid droplets in the SVF at day 7 compared with control treatment, as determined using 4-HNE staining and BODIPY 493/503 staining, respectively, and these changes were prevented by Fer-1 treatment (Figures 2G and 2H).

Having established that ferroptotic signaling reduces lipid droplet contents *in vitro*, we further asked whether it can counteract the expansion of adipose tissue *in vivo*. To investigate this question, we applied a lanolin-based cream containing either RSL3 or vehicle to the skin above the iWAT of HFD-fed mice starting at 8 weeks of an HFD-feeding regimen, and we monitored the mice for body weight (BW) until week 12 (Figure 2I). After 4 weeks of daily application, the whole-BW was lower (Figure 2J), and the BW loss (BW at week 12 minus BW at week 8, Figure 2K) was higher in the RSL3-treated mice compared with the vehicle-treated mice. These differences appear to be due to a decline in eWAT and iWAT mass, as there was no difference in the weights of the liver, heart, spleen, or kidney (Figure 2L) in the RSL3-treated mice compared with the vehicle-treated mice. We also found that 4-HNE staining (Figures 2M and 2N) and MDA content (Figure 2O) were higher in the iWAT of the RSL3-treated mice vs. the vehicle-treated mice, with no difference in the GSH/GSSG ratio (Figure 2P) or in TUNEL staining (Figure 2M), suggesting that the topical application of the ferroptosis agonist RSL3 increases lipid peroxidation/ferroptotic signaling in the underlying iWAT.

By glucose tolerance tests (GTTs) we found that fasted HFD-fed RSL3-treated mice had lower blood glucose levels compared with fasted HFD-fed vehicle-treated mice (Figure 2Q), whereas by insulin tolerance tests (ITTs) we found that there were similar blood glucose levels between fasted HFD-fed RSL3-treated mice and fasted vehicle-treated mice (Figure 2R). Importantly, we found that the degree of oil red O staining of the heart, liver, spleen, and kidney were similar between the two groups (Figures S2A and S2B), suggesting that the prevention of adipose expansion of the eWAT and iWAT by topical RSL3 did not correlate with ectopic lipid deposition in other tissues. Moreover, compared with vehicle-treated mice, the

Figure 2. A non-lethal dose of ferroptosis agonists reduces lipid accumulation

(A) IC_{50} assay for SVFs treated with RSL3 (n = 4).
(B) Cell viability in SVF-derived adipocytes treated as indicated (n = 5–6). For RSL3 treatment, "+" and "++" indicate 30 and 100 nM, respectively.
(C) Images of C11-BODIPY-stained SVFs cultured in adipocyte differentiation medium for 2 days (upper row) or 7 days (lower). Scale bars, 20 μm.
(D–F) MDA content, GSH/GSSG ratio, and oil red O staining in SVF-derived adipocytes (differentiation for 7 days) treated as indicated (n = 5–6).
(G) BODIPY 493/503 staining (green) of SVF-derived adipocytes treated as indicated, and the nuclei were stained with DAPI (blue). Scale bars, 50 μm.
(H) BODIPY 493/503 staining (green) and 4-HNE immunostaining (red) of SVF-derived adipocytes treated as indicated. Scale bars, 20 μm.
(I) A schematic diagram depicting the experimental strategy in which a topical cream containing either RSL3 or vehicle was applied to the skin of HFD-fed mice.
(J–L) BW, BW loss, and tissue weight in HFD-fed mice treated with RSL3- or vehicle-containing cream (n = 11–12).
(M) Representative images of iWAT stained for 4-HNE (left) and TUNEL (right). Scale bars, 100 μm.
(N) 4-HNE-positive iWAT area measured in (M) (n = 5).
(O and P) MDA content and the GSH/GSSG ratio in iWAT (n = 11–12).
(Q and R) GTT and ITT (n = 5).
(S and T) Serum levels of the indicated index (n = 11–12).
Data are presented as mean ± SEM. n.s., not significant; $^{*}p < 0.05$; $^{**}p < 0.01$; $^{***}p < 0.001$ (one-way ANOVA, two-way ANOVA, or unpaired Student's t test).

Please cite this article in press as: Wang et al., Adipocyte-derived ferroptotic signaling mitigates obesity, Cell Metabolism (2024), https://doi.org/10.1016/j.cmet.2024.11.010

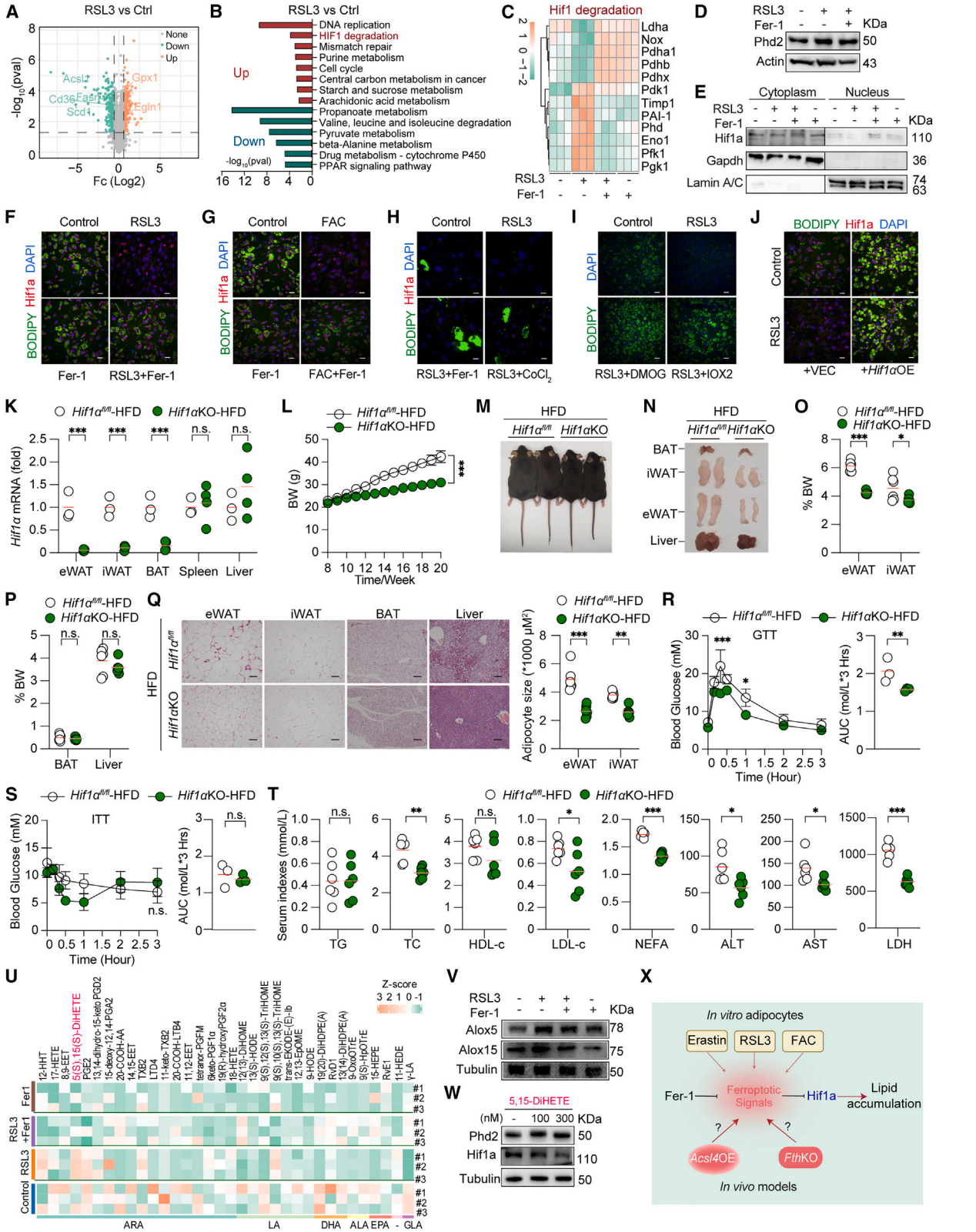

(legend on next page)

RSL3-treated mice had lower levels of total cholesterol (TC), high-density lipoprotein cholesterol (HDL-c), and low-density lipoprotein cholesterol (LDL-c) without a significant change in triglyceride (TG) levels (Figure 2S). Further, topical RSL3 had no significant effect on serum blood urea nitrogen (BUN), alanine transaminase (ALT), aspartate transaminase (AST), albumin (ALB), total protein (TP), creatine kinase (CK), and lactate dehydrogenase (LDH) levels, with the exception of a slight but significant decrease in serum creatinine (CR) levels (Figure 2T), suggesting negligible hepatic and renal toxicity in response to daily application of topical RSL3. Of note, hematological parameters were not affected by topical RSL3 application (Figures S2C and S2D). Together, these results suggest that ferroptotic signaling reduces lipid accumulation *in vitro* and antagonizes adipose expansion *in vivo*, indicating a potentially curative effect against obesity in our HFD-fed mouse model given the degree of weight loss induced by RSL3 treatment after the onset of obesity (Figure 2K).

Ferroptotic signaling reduces fat accumulation by inhibiting HIF1α

Having established that ferroptotic signaling dampens adipose tissue expansion in obese mice, we sought to investigate the underlying mechanism. We performed proteomics analyses (Figure S3A) and identified a total of 159 upregulated proteins and 269 downregulated proteins in RSL3-treated adipocytes differentiated from SVFs compared with control-treated SVFs (Figure 3A). Pathway analysis revealed the enrichment of proteins in the DNA replication, HIF1α degradation, and mismatch repair pathways among the upregulated proteins (Figure 3B). Importantly, these pathways were previously reported to participate in ferroptosis.[28,32–35] We focused on the HIF1α degradation pathway, as HIF1α lies at the intersection between lipid metabolism and ferroptosis,[28] and the HIF1 signaling pathway was predicted as a possible interaction pathway of ferroptosis in obesity, supported by the data analysis above (Figure 1D). Protein levels of Phd2, which mediates HIF1 hydroxylation and degradation,[36] were higher in RSL3-treated SVFs compared with control-treated SVFs (Figures 3C, 3D, and S3B). This finding was consistent with the lower levels of Hif1a protein in the nuclear fraction of RSL3-treated SVFs compared with control-treated SVFs (Figure 3E). Moreover, both BODIPY 493/503 staining and Hif1a (but not Hif2a) immunostaining were significantly lower in RSL3-treated SVFs compared with control-treated SVFs (Figures 3F, S3C, and S3D). Hif1α immunostaining was also lower in FAC-treated SVFs compared with control-treated SVFs (Figures 3G and S3E), suggesting that Hif1a is also inhibited by iron-induced ferroptotic signaling. To validate whether Hif1a is a major target of ferroptotic signaling in regulating lipid droplet content, we co-treated SVFs with RSL3 and $CoCl_2$ (to induce hypoxia, Figures 3H and S3F) or with the PHD2 inhibitors DMOG or IOX2 (Figure 3I), as well as ectopically introducing *Hif1*α using a lentivirus (Figure 3J), and found that such co-treatments restored the lipid droplet content in RSL3-treated SVFs. Together, these data suggested that ferroptotic signaling antagonizes lipid accumulation by reducing Hif1a levels.

Next, we examined the role of Hif1a in adipocytes on adipose expansion by crossing *Adiponectin-Cre* mice (which express Cre recombinase selectively in adipocytes) with *Hif1a*$^{fl/fl}$ mice to generate adipocyte-specific *Hif1a* knockout mice (*Hif1a*KO) with *Hif1a*$^{fl/fl}$ littermates serving as controls. We first confirmed that *Hif1a* expression was depleted in the eWAT, iWAT, and BAT of *Hif1a*KO mice, but was unaffected in the liver and spleen (Figure 3K). Compared with HFD-fed control mice, HFD-fed *Hif1a*KO mice had significantly lower BW gain (Figures 3L and 3M), lower eWAT and iWAT indexes (Figures 3N and 3O) but unchanged BAT and liver index (Figure 3P), reduced adipocyte size, and alleviated fatty liver (Figure 3Q). In addition, by GTTs we found that fasted HFD-fed *Hif1a*KO mice had lower blood glucose levels compared with fasted HFD-fed control mice (Figure 3R), whereas by ITTs we found that there were similar blood glucose levels between fasted HFD-fed *Hif1a*KO mice and fasted HFD-fed control (Figure 3S). Moreover, the HFD-fed *Hif1a*KO mice had lower levels of serum TC, LDL-c, non-esterified fatty acid (NEFA), ALT, AST, and LDH but similar levels of serum TG and HDL-c compared with HFD-fed control mice (Figure 3T).

Figure 3. Ferroptotic signaling reduces fat accumulation by inhibiting Hif1a

(A) Volcano plot of differentially expressed proteins in SVFs cultured in adipocyte differentiation medium for 7 days in the presence or absence of RSL3.
(B) Pathway enrichment analysis of upregulated and downregulated proteins in (A).
(C) Heatmap with unsupervised clustering analysis of differentially expressed proteins in the HIF1 degradation pathway indicated in Figure S3A.
(D and E) Western blot analysis of the indicated protein in SVF-derived adipocytes treated as indicated.
(F–H) Hif1a immunostaining (red) and BODIPY 493/503 staining (green) in SVF-derived adipocytes treated as indicated. Scale bars, 20 μm.
(I) Images of BODIPY 493/503 staining (green) of SVF-derived adipocytes treated as indicated. Scale bars, 50 μm.
(J) Images of Hif1a immunostaining (red) and BODIPY 493/503 staining (green) of SVFs (transduced with *Hif1*α or vector lentivirus) cultured in adipocyte differentiation medium for 7 days in the presence or absence of RSL3. Scale bars, 50 μm.
(K) Summary of *Hif1a* mRNA measured in the tissues of *Hif1a*KO and *Hif1a*$^{fl/fl}$ mice (n = 3–4).
(L) BW curve (n = 6).
(M and N) Representative photographs of HFD-fed *Hif1a*KO and *Hif1a*$^{fl/fl}$ mice.
(O and P) eWAT, iWAT, BAT, and the liver index in HFD-fed *Hif1a*KO and *Hif1a*$^{fl/fl}$ mice (n = 6).
(Q) Images of H&E-stained eWAT, iWAT, BAT, and liver (left) and the quantification of average adipocyte size (right) in eWAT and iWAT obtained from HFD-fed *Hif1a*KO and *Hif1a*$^{fl/fl}$ mice. Scale bars, 100 μm.
(R and S) GTT and ITT (n = 3).
(T) Serum levels of the indicated index (n = 6).
(U) Heatmap analysis of significantly upregulated or downregulated oxylipins in SVF-derived adipocytes. Each oxylipins species was normalized to the corresponding mean value.
(V and W) Western blot analysis of Alox5, Alox15, and tubulin protein in SVF-derived adipocytes.
(X) Scheme of pharmaceutically treatments and potential canonical components of ferroptosis pathways in regulating lipid accumulation via Hif1a.
n.s., not significant; *p < 0.05; **p < 0.01; ***p < 0.001 (two-way ANOVA, or unpaired Student's t test).

Please cite this article in press as: Wang et al., Adipocyte-derived ferroptotic signaling mitigates obesity, Cell Metabolism (2024), https://doi.org/10.1016/j.cmet.2024.11.010

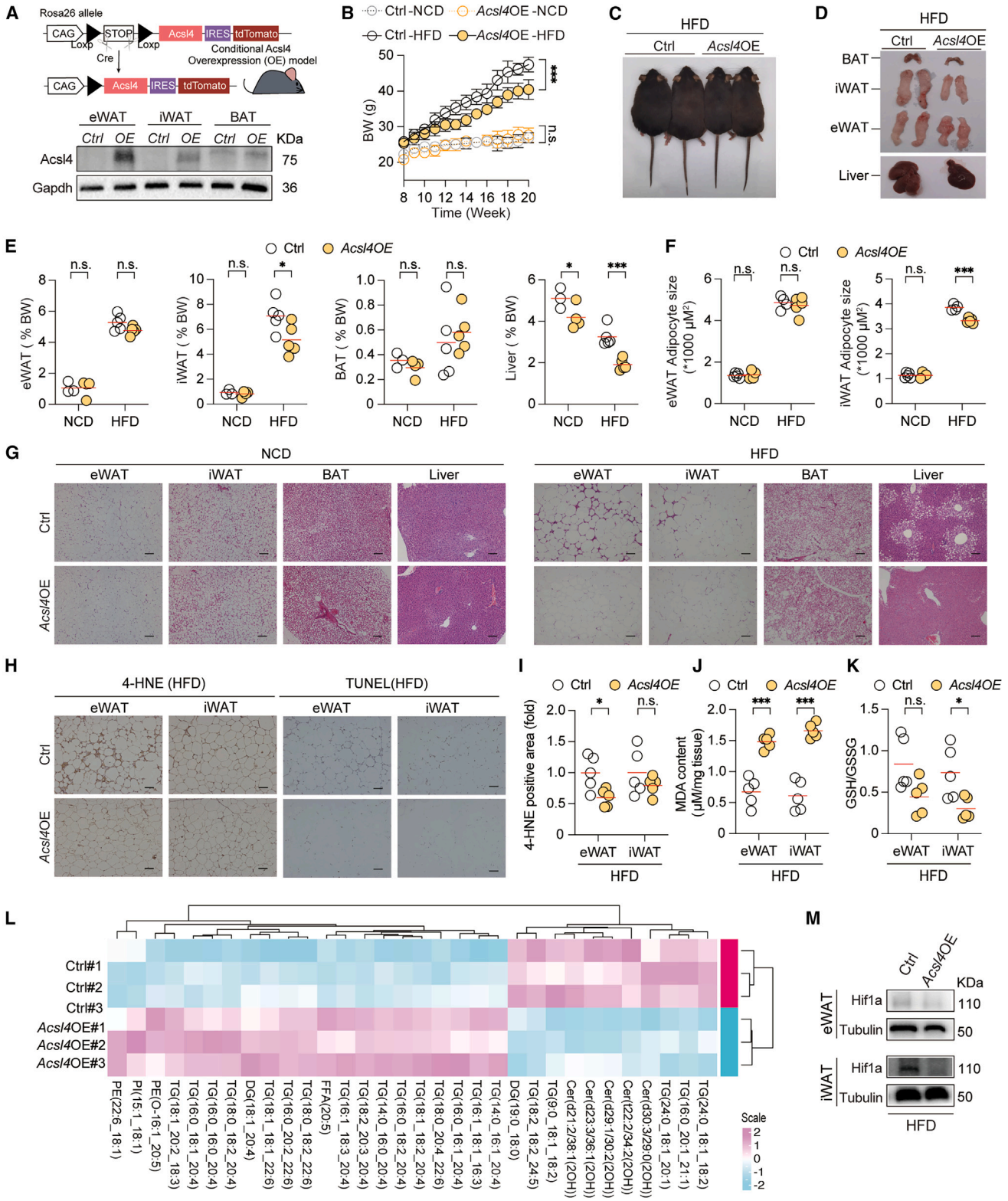

Figure 4. *Acsl4* overexpression in adipocytes ameliorates HFD-induced obesity

(A) Acsl4 protein measured in eWAT, iWAT, and BAT of *Acsl4*OE and Ctrl mice. Upper panel shows the construction strategy of conditional *Acsl4* transgenic mice.

(B) BW curve (n = 4–6).

(C and D) Representative photographs of HFD-fed *Acsl4*OE and Ctrl mice.

(legend continued on next page)

Please cite this article in press as: Wang et al., Adipocyte-derived ferroptotic signaling mitigates obesity, Cell Metabolism (2024), https://doi.org/10.1016/j.cmet.2024.11.010

These findings together with previous reports[37] indicate that the Hif1α pathway in the adipose tissue actively partakes in promoting adipose tissue expansion and compromises the metabolic state during obesity, whose induction may correlate with impaired ferroptotic signaling.

We then asked how ferroptotic signaling acted on Phd2 to reduce Hif1a availability. The induction of ferroptosis requires the oxidation of PUFAs, which further generates bioactive oxylipins.[8,15] We therefore performed oxidative lipidomics to identify differentially produced oxylipins in RSL3-treated SVFs vs. vehicle-treated SVFs (control). This is consistent with the enhanced lipid peroxidation triggered by ferroptosis.[15] Notably, the level of the canonical oxylipins 15-hydroxyeicosatetraenoic acid (15-HETE) and 5-HETE, usually higher in cells undergoing ferroptosis,[15] were not changed in our RSL3-treated SVFs comparing to control (Figure 3U). On the other hand, the level of 5,15-dihydroxyeicosatetraenoic acid (5(S),15(S)-DiHETE), a downstream product of 5-HETE and 15-HETE catalyzed by Alox5 and Alox15, was higher in the RSL3-exposed group compared with the control (Figure 3U). The higher level of 5(S),15(S)-DiHETE in RSL3-treated SVFs may be attributed to the higher protein level of Alox5 and Alox15 in the RSL3-exposed group vs. control (Figure 3V). Importantly, 5(S),15(S)-DiHETE increased the protein level of Phd2 and decreased the protein level of Hif1a in differentiated SVF (Figure 3W). These findings collectively reveal the molecular basis by which ferroptotic signaling inhibits Hif1a in adipocytes. Namely, ferroptotic signaling upregulates the levels of key bioactive lipids that increase the protein levels of Phd2, which in turn destabilizes Hif1a.

Adipocyte-specific overexpression of *Acsl4* induces ferroptotic signaling and alleviates obesity in mice

Having established that pharmacologically induced ferroptotic signaling could mitigate adipose tissue expansion and improve the metabolic state in obesity, we then asked whether other strategies, such as genetic manipulation of the ferroptosis pathway, have similar effects. To achieve this, we genetically manipulated two key genes in canonical pathways controlling ferroptosis (Figure 3X), including lipid peroxidation (*Acsl4*) and iron metabolism (*Fth*).

We first generated adipocyte-specific *Acsl4* overexpression (*Acsl4*OE) mice (Figure 4A), to enforce oxidative lipid production in the adipose tissue. BW gain did not change in NCD-fed *Acsl4*OE mice vs. NCD-fed control (Ctrl) mice, while it was lower in HFD-fed *Acsl4*OE mice vs. HFD-fed control (Ctrl) mice (Figures 4B and 4C). iWAT index and adipocyte size were observed to be lower in HFD-fed *Acsl4*OE mice vs. HFD-fed control (Ctrl) mice (Figures 4D–4G). On the other hand, no differences except for a lower liver index were observed in NCD-fed *Acsl4*OE mice vs. NCD-fed Ctrl mice (Figures 4E–4G). Although there was no significant difference in the eWAT index (Figures 4D and 4E), as well as in adipocyte size (Figures 4F and 4G), eWAT from HFD-fed *Acsl4*OE mice contained fewer crown-like structures than HFD-fed Ctrl mice (Figure 4G), indicating attenuated inflammation and adipose tissue remodeling.[38,39]

Although we found a lower level of 4-HNE staining in the eWAT but no difference in the iWAT from HFD-fed *Acsl4*OE mice vs. control mice (Figures 4H and 4I). The MDA content was higher in the iWAT and the eWAT from HFD-fed *Acsl4*OE mice compared with HFD-fed control mice (Figure 4J), consistent with previous studies showing that *Acsl4* promotes ferroptosis in other tissues.[40–44] The GSH/GSSG ratio was lower in the iWAT and had a lower trend with no significance in the eWAT from HFD-fed *Acsl4*OE mice compared with HFD-fed control mice (Figure 4K). MDA is one of the end products of LOOHs, derived from the decomposition of arachidonic acid (AA) and larger PUFAs.[45] 4-HNE is the major type of 4-hydroxyalkenal end products derived from lipid hydroperoxides of ω-6 fatty acids, including linoleic acid and AA.[45] The discrepancies with respect to different levels of lipid peroxidation byproducts in HFD-fed *Acsl4*OE mice might reflect the selectivity of Acsl4 in catalyzing lipids.[46,47] In support of this notion, we performed lipidomics to decipher the lipid profile in the iWAT of HFD-fed *Acsl4*OE mice vs. control mice. Supporting a role for ACSL4, which prefers 20-carbon PUFA substrates, and along with other ACSLs that have been associated with the cellular uptake of exogenous fatty acids,[48] we found that free 20:5 and 20:5-containing phosphatidyl ethanolamine (PE) were more abundant in the iWAT from HFD-fed *Acsl4*OE mice vs. control mice (Figure 4L). Similarly, 20:4 and 22:4 (AA and adrenic acid [AdA])-containing TG and diacylglycerol (DG) species were more abundant in the iWAT from HFD-fed *Acsl4*OE mice vs. control mice (Figure 4L). The peroxide products of these PEs (Figure 4L) could be mediators for ferroptotic signaling.[46,49] Furthermore, we noticed that the eWAT and the iWAT from HFD-fed *Acsl4*OE mice did not have overt cell death as determined by an unchanged TUNEL staining (Figure 4H), cleaved-caspase3 protein level (Figures S4A and S4B), and caspase 3 activity (Figure S4C). More importantly, we observed a reduction of Hif1a protein levels in the iWAT but not the eWAT from HFD-fed *Acsl4*OE mice vs. control mice (Figure 4M), reinforcing the notion that ferroptotic signaling suppresses Hif1a availability to control adipose tissue expansion during obesity. These data suggest that *Acsl4* overexpression in the adipose tissue did not cause significant ferroptotic cell death but rather specifically enhanced the ferroptotic signaling.

(E) eWAT, iWAT, BAT, and the liver index (n = 3–6).
(F) Quantification of average adipocyte size measured as shown in (G) (n = 4–6).
(G) H&E-stained eWAT, iWAT, BAT, and liver samples. Scale bars, 100 μm.
(H) Images of eWAT and iWAT samples obtained from HFD-fed *Acsl4*OE and Ctrl mice stained for 4-HNE (left) and TUNEL (right). Scale bars, 100 μm.
(I) 4-HNE—positive area in eWAT and iWAT sections measured as shown in (H) (n = 5).
(J and K) MDA content and the GSH/GSSG ratio in eWAT and iWAT obtained from HFD-fed *Acsl4*OE and Ctrl mice (n = 5).
(L) Heatmap unsupervised clustering analysis of differentially expressed lipids in iWAT from HFD-fed *Acsl4*OE and Ctrl mice (n = 3).
(M) Western blot analysis of Hif1a and β-tubulin protein in eWAT (top) and iWAT (bottom) obtained from HFD-fed *Acsl4*OE and Ctrl mice.
Data are represented as mean ± SEM in (B). n.s., not significant; *p < 0.05; ***p < 0.001 (two-way ANOVA).

Please cite this article in press as: Wang et al., Adipocyte-derived ferroptotic signaling mitigates obesity, Cell Metabolism (2024), https://doi.org/10.1016/j.cmet.2024.11.010

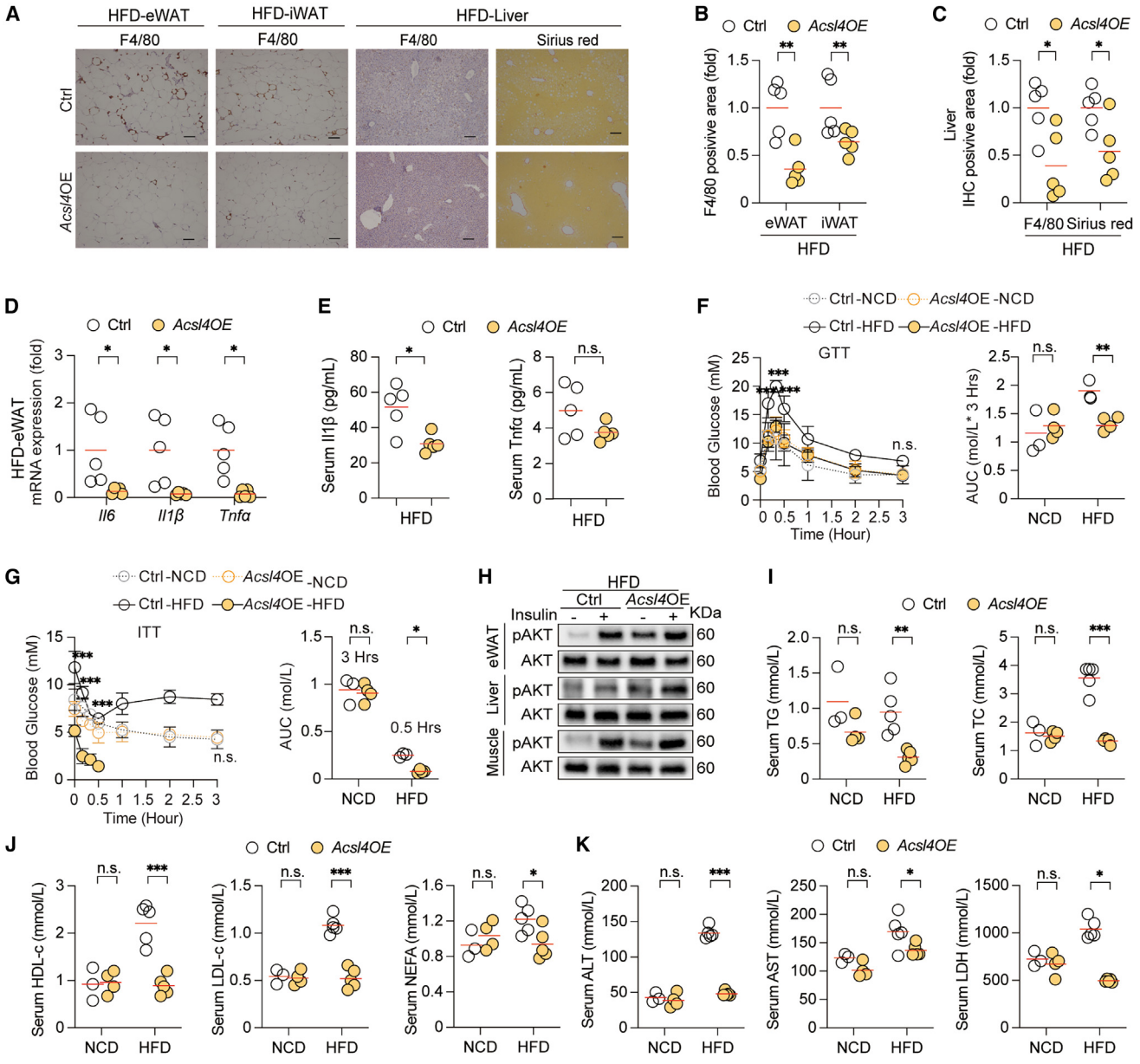

Figure 5. *Acsl4* overexpression in adipocytes alleviates metabolic disorder

(A–C) Images and quantification of F4/80- or Sirius red-positive area from eWAT, iWAT, and liver samples obtained from HFD-fed *Acsl4*OE and Ctrl mice. Scale bars, 100 μm.

(D) mRNA expression of indicated proinflammatory gene (n = 5).

(E) Serum levels of the indicated proinflammatory cytokines (n = 5).

(F and G) GTT and ITT (n = 3–5).

(H) Western blot analysis of p-AKT in eWAT, liver, and muscle of HFD-fed *Acsl4*OE and Ctrl mice after intravenous injection of saline (–) or insulin (1.5 U kg^{-1}).

(I–K) Serum levels of the indicated index (n = 3–5).

n.s., not significant; *p < 0.05; **p < 0.01; ***p < 0.001 (two-way ANOVA, or unpaired Student's t test).

We observed a lower level of F4/80 immunostaining (Figures 5A and 5B) and nuclear factor (Nf)-κb protein levels (Figure S5A) in adipose tissues, as well as lower levels of F4/80 immunostaining and Sirius red staining in the liver from HFD-fed *Acsl4*OE mice compared with HFD-fed control mice (Figures 5A and 5C). In line with this notion, we found lower proinflammatory cytokines (Il-6, Il-1β, and tumor necrosis factor alpha [Tnf-α]) mRNA expression (Figure 5D) in adipose tissues and lower circulation protein levels of IL-1β while no change of circulation protein level of Tnf-α (Figure 5E). These data suggest that *Acsl4* overexpression in the adipose tissue does not cause significant tissue inflammation.

We then asked whether *Acsl4* overexpression affects the metabolic state during HFD feeding. We found that blood

Please cite this article in press as: Wang et al., Adipocyte-derived ferroptotic signaling mitigates obesity, Cell Metabolism (2024), https://doi.org/10.1016/j.cmet.2024.11.010

CellPress
OPEN ACCESS

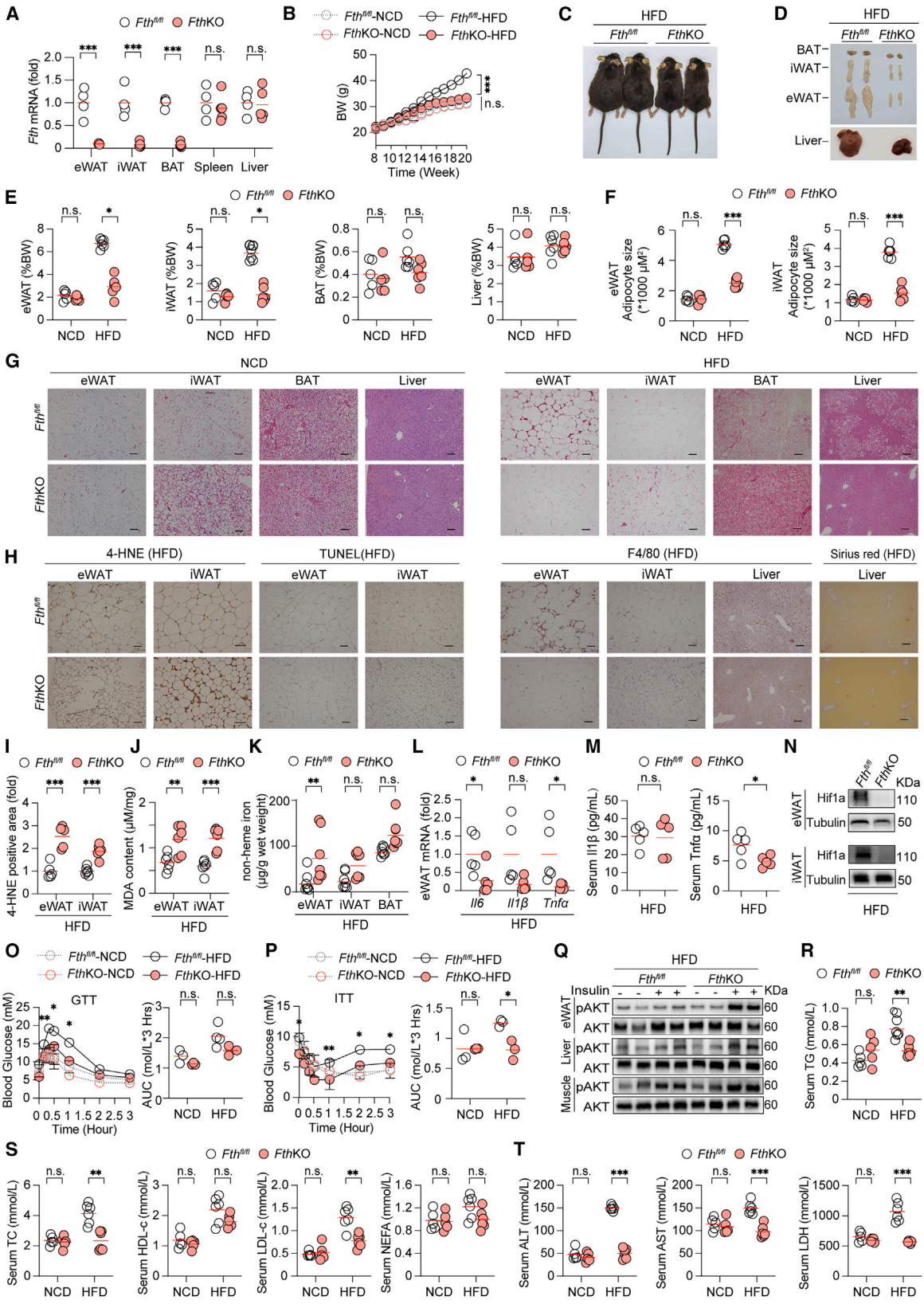

(legend on next page)

Please cite this article in press as: Wang et al., Adipocyte-derived ferroptotic signaling mitigates obesity, Cell Metabolism (2024), https://doi.org/10.1016/j.cmet.2024.11.010

glucose levels were lower during both GTTs (Figure 5F) and ITTs (Figure 5G) in fasted HFD-fed *Acsl4*OE compared with fasted HFD-fed control mice, indicating an improved metabolic state in HFD-fed *Acsl4*OE mice. Of note, HFD-fed *Acsl4*OE mice were sensitive to insulin as they fainted 30 min after insulin inoculation during the ITT. Therefore, the glucose measurements after 30 min were terminated. Consistent with these findings, we found that even when without insulin challenge, the phosphorylation level of Akt (p-AKT) was significantly higher in the eWAT, liver, and skeletal muscle of HFD-fed *Acsl4*OE mice vs. HFD-fed control mice (Figure 5H), suggesting an improved insulin sensitivity even at baseline. In addition, compared with HFD-fed control mice, HFD-fed *Acsl4*OE mice had lower serum TG, TC, HDL-c, LDL-c, NEFA, ALT, AST, and LDH levels (Figures 5I–5K). On the other hand, we found no difference in these serum parameters between NCD-fed *Acsl4*OE mice and NCD-fed control (Figures 5I–5K). To disentangle the main driver of the reduced plasma lipids in the HFD-fed *Acsl4*OE mice vs. the HFD-fed control mice, mice were administrated with tyloxapol, a lipoprotein lipase inhibitor. We found that TG levels were higher in HFD-fed *Acsl4*OE mice vs. HFD-fed control mice (Figure S5B). These data indicate that HFD-fed *Acsl4*OE mice have lower plasma lipids despite higher TG secretion from the liver, suggesting an enhanced lipid clearance capacity of *Acsl4*OE mice. These data provide supporting evidence that ferroptotic signaling elicited by *Acsl4* overexpression enables a stronger lipid clearance capacity and promotes insulin sensitivity, thereby counteracting the effect of adipose tissue expansion and the progression of metabolic disorders during obesity.

Loss of *Fth* in adipocytes induces ferroptotic signaling and alleviates obesity in mice

We then asked whether iron-derived ferroptotic signaling regulates adipose tissue expansion in obesity. We thus generated adipocyte-specific *Fth* knockout (*Fth*KO) mice by crossing *Adiponectin-Cre* mice with $Fth^{fl/fl}$ mice. We confirmed the depletion of *Fth* in the eWAT, iWAT, and BAT (Figure 6A). We observed no difference in terms of BW gain in NCD-fed *Fth*KO mice compared with NCD-fed $Fth^{fl/fl}$ mice (Figure 6B). By contrast, compared with HFD-fed control mice, HFD-fed *Fth*KO mice had reduced weight gain (Figures 6B and 6C), a lower fat index (Figures 6D and 6E), reduced adipocyte size (Figure 6F and 6G), and reduced fatty liver (Figure 6G). Of note, NCD-fed *Fth*KO mice and NCD-fed $Fth^{fl/fl}$ mice had similar fat index (Figure 6E), adipocyte size (Figures 6F and 6G), and liver histology (Figure 6G).

Consistent with previous studies showing that Fth negatively regulates ferroptosis in other cell types in mice,[15,50] we detected increased levels of ferroptotic signaling in the eWAT and iWAT in HFD-fed *Fth*KO mice compared with HFD-fed control mice, as demonstrated by increased 4-HNE staining (Figures 6H and 6I) and MDA content (Figure 6J). There was no difference in the GSH/GSSG ratio between these two groups (Figure S6A). We also observed no difference in non-heme iron content in the eWAT, iWAT, or BAT between NCD-fed *Fth*KO mice and NCD-fed control (Figure S6B). By contrast, we found higher non-heme iron content in the eWAT but not iWAT (Figure 6K) of HFD-fed *Fth*KO mice compared with HFD-fed control mice. Considering that Fth controls the labile iron pool in a variety of organs,[15,51,52] the enhanced ferroptotic signaling in HFD-fed *Fth*KO mice is probably attributed to the unleashed labile iron.

Furthermore, we found that the eWAT and iWAT from HFD-fed *Fth*KO mice did not have overt cell death as determined by TUNEL staining (Figure 6H), cleaved-caspase3 protein level (Figure S6C) and caspase 3 activity (Figure S6D), and did not have tissue inflammation despite the accumulation of lipid peroxidation, as shown by lower F4/80 immunostaining in the eWAT and iWAT (Figures 6H and S6E), lower Nf-κb protein level in the eWAT (Figure S6F), lower proinflammatory cytokines (Il-6 and Tnf-α) mRNA expression in the eWAT (Figure 6L), and lower circulation protein levels of Tnf-α while no change of circulation protein level of IL-1β (Figure 6M). Moreover, HFD-fed *Fth*KO mice had lower levels of F4/80 immunostaining and Sirius red staining in the liver than control mice (Figures 6H and S6G). These data suggest that similar to *Acls4*OE, *Fth*KO in the adipose tissue did not cause significant ferroptotic cell death and tissue inflammation but rather enhanced the ferroptotic signaling. More importantly, we observed a reduction of Hif1a protein level both in the iWAT and eWAT from HFD-fed *Fth*KO mice vs. control mice (Figure 6N), suggesting that labile iron elicited ferroptotic signaling may suppress Hif1a availability to control adipose expansion during obesity.

Figure 6. *Fth* in adipocytes contributes to adipose tissue expansion in HFD-induced obesity

(A) *F*th mRNA measured in tissues of *Fth*KO and $Fth^{fl/fl}$ mice (n = 4–5).
(B) BW curve (n = 5–6).
(C and D) Representative photographs of HFD-fed *Fth*KO and $Fth^{fl/fl}$ mice.
(E) eWAT, iWAT, BAT, and the liver index (n = 5–6).
(F) Quantification of average adipocyte size in eWAT and iWAT as shown in (G) (n = 5–6).
(G) H&E-stained eWAT, iWAT, BAT, and liver samples. Scale bars, 100 μm.
(H) Images of eWAT, iWAT, and liver samples obtained from HFD-fed *Fth*KO and $Fth^{fl/fl}$ mice and stained for 4-HNE, TUNEL, F4/80, or Sirius red. Scale bars, 100 μm.
(I) 4-HNE—positive area in eWAT and iWAT sections measured as shown in (H) (n = 6).
(J) MDA content (n = 6).
(K) Non-heme iron content (n = 6).
(L) mRNA expression of indicated proinflammatory gene (n = 5).
(M) Serum levels of the indicated proinflammatory cytokines (n = 5).
(N) Western blot analysis of Hif1a and β-tubulin protein in eWAT (top) and iWAT (bottom) obtained from HFD-fed *Fth*KO and $Fth^{fl/fl}$ mice.
(O and P) GTT and ITT (n = 3–4).
(Q) Western blot analysis of p-AKT in eWAT, liver, and muscle of HFD-fed *Fth*KO and $Fth^{fl/fl}$ mice after intravenous injection of saline (−) or insulin (1.5 U kg^{-1}).
(R–T) Serum levels of the indicated index (n = 5–6).
n.s., not significant; $^{*}p < 0.05$; $^{**}p < 0.01$; $^{***}p < 0.001$ (one-way ANOVA, two-way ANOVA, or unpaired Student's t test).

Please cite this article in press as: Wang et al., Adipocyte-derived ferroptotic signaling mitigates obesity, Cell Metabolism (2024), https://doi.org/10.1016/j.cmet.2024.11.010

CellPress
OPEN ACCESS

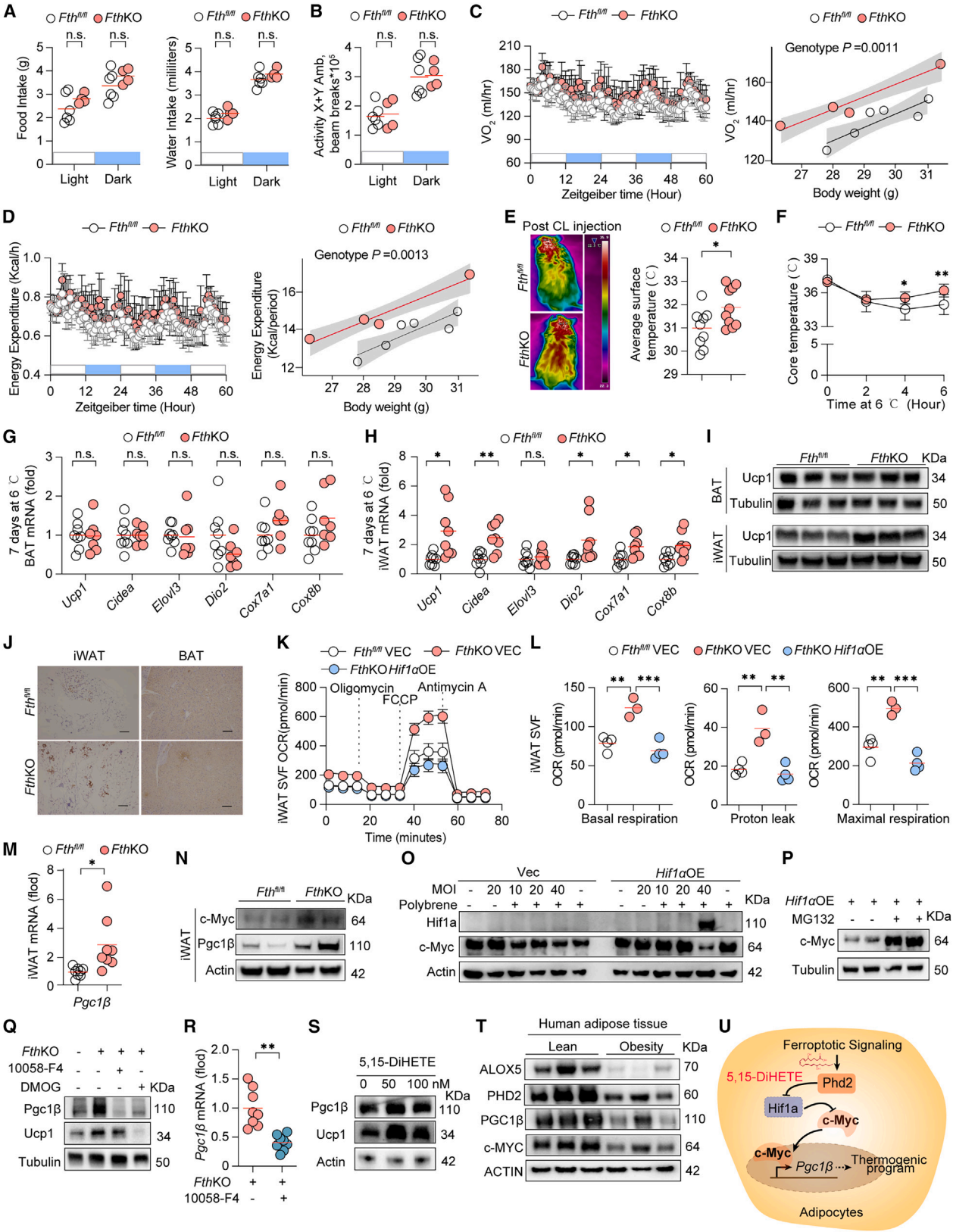

(legend on next page)

Please cite this article in press as: Wang et al., Adipocyte-derived ferroptotic signaling mitigates obesity, Cell Metabolism (2024), https://doi.org/10.1016/j.cmet.2024.11.010

Blood glucose levels were lower during both GTTs (Figure 6O) and ITTs (Figure 6P) in fasted HFD-fed *Fth*KO mice compared with fasted HFD-fed control mice, indicating an improved metabolic state in HFD-fed *Fth*KO mice. We observed a higher p-AKT protein in eWAT, liver, and skeletal muscle of insulin-treated HFD-fed *Fth*KO mice vs. HFD-fed control mice (Figure 6Q), suggesting an improved insulin sensitivity. HFD-fed *Fth*KO mice had lower serum TG, TC, LDL-c, ALT, AST, and LDH levels but similar levels of serum HDL-c and NEFA compared with HFD-fed control mice (Figures 6R–6T). On the other hand, we found no difference in these serum parameters between NCD-fed *Fth*KO mice and NCD-fed control (Figures 6R–6T). HFD-fed *Fth*KO mice also had stronger lipid clearance compared with HFD-fed control mice, as supported by lower plasma lipids despite higher serum TG levels after tyloxapol administration in fasted HFD-fed *Fth*KO mice (Figure S6H). These data suggest that ferroptotic signaling elicited by unleashed labile iron enables a stronger lipid clearance capacity and promotes insulin sensitivity, thereby counteracting the effects of adipose tissue expansion and the progression of metabolic disorders during obesity.

Fth restrains beige fat thermogenesis by inhibiting a c-Myc-Pgc1β pathway

To further investigate the mechanism by which adipocyte-derived ferroptotic signaling ameliorates obesity, we first questioned whether the communication between adipocytes and macrophages was rewired by *F*th deletion specifically in the adipocytes, given that aberrant adipose macrophages are closely associated with obesity[53] and global *Fth* depletion in adult mice triggers leukocytes infiltration and white adipose tissue atrophy.[54] We therefore dissected the profiles of adipose tissue macrophages from *Fth*KO mice fed a HFD for 2 months (Figures S7A and S7B). We found no difference between *Fth*KO and control mice with respect to the percentage or absolute number of $CD11c^{+}CD206^{-}$, $CD11c^{+}CD206^{+}$, $CD11c^{-}CD206^{+}$, or $CD9^{+}$ macrophages in both the eWAT and iWAT (Figure S7A), suggesting that Fth in adipocytes does not play a major role in regulating the interaction between adipocytes and macrophages.

We then found that HFD-fed *Fth*KO mice had similar food intake, water intake, and activity but had a higher O_2 consumption rate and energy expenditure compared with HFD-fed control mice (Figures 7A–7D). When challenged with CL-316,214 (a β3-adrenergic receptors agonist used as a pharmacologic activator of thermogenic fat),[55–57] HFD-fed *Fth*KO mice presented with significantly higher surface temperatures than control mice (Figure 7E). Meanwhile, *Fth*KO mice under HFD feeding for 1 month had a stronger capacity to maintain their body temperature upon cold exposure compared with control mice (Figure 7F). These results prompted us to hypothesize that Fth in adipocyte reduces energy expenditure by restraining adaptive thermogenesis. In support of this notion, thermogenic genes and mitochondrial genes were not changed in the BAT (Figures 7G and S7C), while were markedly higher in the iWAT (Figures 7H and S7D) of HFD-fed *Fth*KO mice compared with HFD-fed control mice following cold exposure at 6°C for 1 week. Meanwhile, we found no significant compensation by non-shivering thermogenesis in the skeletal muscle (Figure S7E). The levels of uncoupling protein 1 (Ucp1) protein were more pronounced in the iWAT but not the BAT of *Fth*KO mice vs. control mice under HFD feeding for 1 month, following 1 week of cold exposure (Figures 7I, 7J, and S7F). Measurement of the oxygen consumption rate (OCR) further revealed significantly higher basal and maximal levels of mitochondrial respiration, as well as proton leak, in differentiated SVFs isolated from the iWAT (Figures S7G and S7H) but not the BAT (Figures S7I and S7J) in *Fth*KO mice when compared with cells from control mice. Notably, forced *Hif1a* expression via lentivirus reversed the elevated OCR in differentiated SVFs isolated from the iWAT of *Fth*KO mice (Figures 7K and 7L). Together, these data demonstrate a critical role of Fth in adipocytes in repressing cold-induced beiging of the iWAT.

We then asked how ferroptotic signaling activates adipose thermogenesis. Pgc1β is a key transcriptional co-activator that

Figure 7. Deletion of *Fth* augments thermogenesis in white adipocytes

(A and B) Average food intake and water intake (A) and activities (B) measured in HFD-fed *Fth*KO and $Fth^{fl/fl}$ mice. In this figure, mice fed with HFD began at 6 weeks old and continued for 1 month (n = 4–6).

(C and D) O_2 consumption and energy expenditure measured in HFD-fed *Fth*KO and $Fth^{fl/fl}$ mice (n = 4–6).

(E) Representative infrared images (left) and the average body surface temperature (right) of HFD-fed *Fth*KO and $Fth^{fl/fl}$ mice following 6.5 h of CL-316,243 injection (n = 9–10).

(F) Body temperature of HFD-fed *Fth*KO and $Fth^{fl/fl}$ mice during acute cold exposure (n = 4–6).

(G and H) mRNA expression of the indicated thermogenic genes in BAT (G) and iWAT (H) from HFD-fed *Fth*KO and $Fth^{fl/fl}$ mice after 7 d cold exposure at 6°C (n = 7–8).

(I) Western blot analysis of Ucp1 and tubulin in BAT (top) and iWAT (bottom) obtained from HFD-fed *Fth*KO and $Fth^{fl/fl}$ mice after 7 d cold exposure at 6°C (n = 3).

(J) Representative UCP1 immunostaining of BAT and iWAT sections. Scale bar, 100 μm.

(K and L) SVF cells isolated from iWAT of either $Fth^{fl/fl}$ mice or *Fth*KO mice were cultured *in vitro*. The 30% confluency cells were infected with indicate lentivirus for 20 h, then induced differentiation toward adipocytes. Oxygen consumption rates (OCRs) of adipocytes with indicated treatments were detected. OCRs were normalized to the cell viability. Data represent mean ± SD at each time point (K) and mean (L) (n = 3–4).

(M and N) mRNA expression of *Pgc1β* (M) and western blot analysis of the indicated protein (N) measured in iWAT obtained from HFD-fed *Fth*KO and $Fth^{fl/fl}$ mice after 7 d cold exposure at 6°C (n = 7–8).

(O) Western blot analysis of Hif1α, c-Myc, and actin proteins in SVFs infected with indicated lentivirus.

(P) Western blot analysis of c-Myc and tubulin proteins in SVFs infected with lentivirus-mediated overexpression of Hif1a with 10 mM MG132 or vehicle (DMSO) for the last 4 h.

(Q) Western blot analysis of Pgc1β, Ucp1, and tubulin proteins in SVF-derived adipocytes. SVF cells isolated from iWAT of either $Fth^{fl/fl}$ mice or *Fth*KO mice.

(R) mRNA expression of *Pgc1β* measured in SVF-derived adipocytes, with/without 10058-F4 (70 μM). SVFs isolated from iWAT of *Fth*KO mice.

(S) Western blot analysis of Pgc1β, Ucp1, and actin proteins in SVF-derived adipocytes. SVF cells isolated from iWAT of wild-type mice.

(T) Western blot analysis of the indicated protein in abdominal adipose lysates obtained from individuals with obesity vs. lean condition (n = 3).

(U) Scheme of how ferroptotic signaling enhances thermogenesis.

n.s., not significant; $^{*}p < 0.05$; $^{**}p < 0.01$; $^{***}p < 0.001$ (one-way ANOVA, two-way ANOVA, or unpaired Student's t test).

controls adaptive thermogenesis and mitochondrial oxidative energy metabolism.[56,58–60] Zhang et al. reported that HIF1 inhibits *PGC1β* mRNA expression by repressing c-Myc activity.[61] We found the mRNA expression of *Pgc1β* (Figure 7M), as well as the protein expressions of c-Myc and Pgc1β (Figures 7N and S7K), were higher in the iWAT from HFD-fed *Fth*KO mice than those in HFD-fed control mice following cold exposure at 6°C for 1 week. We therefore hypothesized that ferroptotic signaling-induced reductions in Hif1a levels promote c-Myc expression, thereby rejuvenating Pgc1β expression. In support of this notion, forced Hif1a expression suppressed the protein level of c-Myc in SVFs in a proteasome-dependent manner (Figures 7O and 7P) as proteasome inhibitor (MG132) reversed the protein level of c-Myc in *Hif1a*OE SVFs, in line with a previous study.[61] 10058-F4, a selective small molecule inhibitor of c-Myc, suppressed both the protein levels and mRNA expression of Pgc1β as well as the protein levels of Ucp1 in adipocytes differentiated from SVFs isolated from the iWAT of *Fth*KO mice (Figures 7Q and 7R). In addition, DMOG suppressed the protein level of Pgc1β and Ucp1 in adipocytes differentiated from SVFs isolated from the iWAT of *Fth*KO mice (Figure 7Q). These results suggest that Hif1a may act as a critical factor to constrain the thermogenic program in beige adipocytes, while ferroptotic signaling may negatively target a Hif1a-c-Myc-Pgc1β pathway to rewire systemic energy metabolism into a thermogenic shunt.

We then found that adding 5(S),15(S)-DiHETE increased the protein levels of Pgc1β and Ucp1 (Figure 7S) in adipocytes differentiated from SVFs isolated from the iWAT, which further supports the notion that enhanced ferroptotic signaling boosts thermogenesis. Notably, the protein levels of ALOX5, PHD2, PGC1β, and c-MYC were lower in the abdominal adipose tissue from individuals with obesity vs. lean controls (Figures 7T and S7L). These data imply an underappreciated link between a HIF1 signaling-thermogenesis axis and ferroptotic signaling in human obesity (Figure 7U). Taken together, these findings suggest that activation of ferroptotic signaling in adipose tissue can boost thermogenesis in adipocytes, conferring protection against diet-induced obesity.

DISCUSSION

Excessive oxidative stress in white adipose tissue usually links to metabolic dysfunction in HFD-feeding models. However, moderate levels of oxidative stress in the white adipose tissue could improve metabolic disorder[62] and increase glucose uptake and thermogenesis in the WAT.[63–67] We show that ferroptotic signaling mediated by 5,15-dihydroxyeicosatetraenoic acid (5,15-DiHETE) in adipocytes helps prevent adipose tissue expansion and the development of metabolic disorders in the context of obesity.

Our findings suggest that ferroptotic signaling derived from lipid peroxidation accumulation, cystine deprivation, and/or iron accumulation has similar effects *in vitro*. Further, our *in vivo* data indicate that the upregulation of *Fth* in obesity is probably a maladaptive response.[16] This hypothesis is consistent with previous studies showing that ferritin levels are increased in individuals with obesity.[68,69] Interestingly, HFD-fed *Fth*KO or HFD-fed *Acsl4*OE mice did not show overt cell death in the WAT. These could be explained by (1) other salvage pathways that may kick in, such as Gpx4, Fsp1, etc. and (2) other cell types in the adipose tissue may help support tissue homeostasis when the oxidative balance is perturbed in adipocyte.[54,70,71]

Activation of hypoxic signaling and the accumulation of HIF1α have been well described in 3T3-L1 cells, obese mice, and individuals with obesity.[37,72–75] Here, we show that knocking out *Hif1a* in adipocytes via *Adipoq-Cre* reduces adipose expansion and protects against HFD-induced obesity in mice. We found that Hif1a inhibits WAT beiging by repressing a c-Myc-PGC1β pathway. These findings support our hypothesis that the reduction of HIF1α protein contributes to preventing adipose expansion.

The activated thermogenic program in HFD-fed *Fth*KO delayed temperature loss at an early stage (before 6 h) of cold exposure. Although it is well established that beige adipocytes and brown adipocytes respond to cold exposure synergistically, the correlation between the two is rather complex. There are studies showing that beige adipocytes do not contribute to thermogenesis during the early stages of cold exposure,[76] whereas other studies reported the altered thermogenic capacity during the early stages of cold exposure occurs when only beige adipocytes are affected.[56,57,66] These studies collectively reveal the complexity of the interplay between beige adipocytes and brown adipocytes. It is also worth noting that ferroptotic signaling has more of an impact on the iWAT vs. the BAT. We reason that brown adipocytes have a greater exposure to iron availability or have a greater capacity for iron uptake than beige adipocytes.[12] Therefore, depleting *Fth* may not be able to further boost the thermogenic capacity in the BAT. While in the iWAT, given that the iron content is relatively lower than in the BAT under steady state as well as upon HFD-feeding, depleting *Fth* in adipose tissues may result in more susceptibility of the iWAT to ferroptotic signaling, thereby enhancing thermogenesis in the iWAT.

Compared with NCD feeding, HFD feeding induces insulin resistance, leading to hyperinsulinemia.[77] Thus, HFD-fed *Acsl4*OE mice could secrete more insulin, which causes them to faint after insulin inoculation during our ITTs. In summary, our findings suggest that FTH, ACSL4, and/or ferroptotic signaling may serve as potential therapeutic targets for reducing obesity.

Limitations of the study

Although we showed that ferroptotic signaling mitigates obesity using multiple mouse models, more evidence is needed to confirm the dependency of ferroptotic signaling in regulating adipose expansion and thermogenesis. It is still unclear how bioactive lipids act on Phd2 to regulate Hif1a levels. We envision that ferrology, with multiple interdisciplinary technologies, will have a large impact on the ability to empower the precise manipulation of ferroptosis and iron to allow for the better management of disease conditions.[78]

RESOURCE AVAILABILITY

Lead contact

Further information and requests for resources and reagents should be directed to and will be fulfilled by the lead contact, Fudi Wang (fwang@zju.edu.cn).

Materials availability

This study did not generate new, unique reagents.

Data and code availability

- All data reported in this study are available from the lead contact upon request. All raw data used to generate the figures throughout the manuscript can be found within the Data S1 document. All raw oxylipins and lipidomics datasets have been uploaded into Mendeley Data (https://data.mendeley.com/datasets/9h9b224k26/1).
- This paper does not report original code.
- Any additional information required to reanalyze the data reported in this paper is available from the lead contact upon request.

The datasets supporting the conclusions of this article are included within the article and its additional files. The primary data that support the findings of this study are not openly available due to patient privacy. Access can be granted by contacting Fudi Wang (fwang@zju.edu.cn) and requires a data-access agreement, and requests will be replied to within 4 weeks. Zhejiang University School of Medicine securely stores all primary data with controlled access. Source data are provided in this paper.

ACKNOWLEDGMENTS

This study was supported by grants from the National Natural Science Foundation of China (32330047 and 31930057 to F.W., 82471593 to J.M., 32300988 to Xue Wang, and 32171166 and 82030003 to Q.W.) and the China Postdoctoral Science Foundation (2022M712733 to Xue Wang). The authors thank Dr. Hong Gao from Wuhan University and Dr. Xiaoying Li from Zhongshan Hospital at Fudan University for helpful discussions.

AUTHOR CONTRIBUTIONS

F.W., Xue Wang, Q.W., and J.M. conceived the study and wrote the manuscript. Xue Wang, Q.W., Xinhui Wang, F.W., and J.M. designed experiments. Xue Wang, Q.W., M.Z., Y.W., X.L., W.Z., C.G., Xinhui Wang, Y.Y., S.Y., T.W., E.X., and W.S. performed experiments and analyzed the data. Y.C. collected clinical samples. F.W. and J.M. revised the manuscript and supervised the study.

DECLARATION OF INTERESTS

The authors declare no competing interests.

STAR★METHODS

Detailed methods are provided in the online version of this paper and include the following:

SUPPLEMENTAL INFORMATION

Supplemental information can be found online at https://doi.org/10.1016/j.cmet.2024.11.010.

Received: March 26, 2024
Revised: September 29, 2024
Accepted: November 12, 2024
Published: December 26, 2024

REFERENCES

1. Shaikh, S.R., Beck, M.A., Alwarawrah, Y., and MacIver, N.J. (2024). Emerging mechanisms of obesity-associated immune dysfunction. Nat. Rev. Endocrinol. *20*, 136–148. https://doi.org/10.1038/s41574-023-00932-2.
2. Wang, X., Zhou, Y., Min, J., and Wang, F. (2023). Zooming in and out of ferroptosis in human disease. Front. Med. *17*, 173–206. https://doi.org/10.1007/s11684-023-0992-z.
3. Ru, Q., Li, Y., Chen, L., Wu, Y., Min, J., and Wang, F. (2024). Iron homeostasis and ferroptosis in human diseases: mechanisms and therapeutic prospects. Signal Transduct. Target. Ther. *9*, 271. https://doi.org/10.1038/s41392-024-01969-z.
4. Sun, S., Shen, J., Jiang, J., Wang, F., and Min, J. (2023). Targeting ferroptosis opens new avenues for the development of novel therapeutics. Signal Transduct. Target. Ther. *8*, 372. https://doi.org/10.1038/s41392-023-01606-1.
5. Fang, X., Ardehali, H., Min, J., and Wang, F. (2023). The molecular and metabolic landscape of iron and ferroptosis in cardiovascular disease. Nat. Rev. Cardiol. *20*, 7–23. https://doi.org/10.1038/s41569-022-00735-4.
6. Shen, J., Xie, E., Shen, S., Song, Z., Li, X., Wang, F., and Min, J. (2024). Essentiality of SLC7A11-mediated nonessential amino acids in MASLD. Sci. Bull. (Beijing). https://doi.org/10.1016/j.scib.2024.09.019.
7. Shao, T., and Chung, R.T. (2024). Ironing out MAFLD: therapeutic targeting of liver ferroptosis. Cell Metab. *36*, 2167–2169. https://doi.org/10.1016/j.cmet.2024.09.005.
8. Stockwell, B.R. (2022). Ferroptosis turns 10: Emerging mechanisms, physiological functions, and therapeutic applications. Cell *185*, 2401–2421. https://doi.org/10.1016/j.cell.2022.06.003.
9. Ma, W., Jia, L., Xiong, Q., and Du, H. (2021). Iron overload protects from obesity by ferroptosis. Foods *10*, 1787. https://doi.org/10.3390/foods10081787.
10. Kitamura, N., Yokoyama, Y., Taoka, H., Nagano, U., Hosoda, S., Taworntawat, T., Nakamura, A., Ogawa, Y., Tsubota, K., and Watanabe, M. (2021). Iron supplementation regulates the progression of high fat diet induced obesity and hepatic steatosis via mitochondrial signaling pathways. Sci. Rep. *11*, 10753. https://doi.org/10.1038/s41598-021-89673-8.
11. Mai, X., Liu, Y., Fan, J., Xiao, L., Liao, M., Huang, Z., Chen, Z., Huang, S., Sun, R., Jiang, X., et al. (2024). Iron supplementation and iron accumulation promote adipocyte thermogenesis through PGC1α-ATGL-mediated lipolysis. J. Biol. Chem. *300*, 107690. https://doi.org/10.1016/j.jbc.2024.107690.
12. Li, J., Pan, X., Pan, G., Song, Z., He, Y., Zhang, S., Ye, X., Yang, X., Xie, E., Wang, X., et al. (2020). Transferrin receptor 1 regulates thermogenic capacity and cell fate in brown/beige adipocytes. Adv. Sci. (Weinh) *7*, 1903366. https://doi.org/10.1002/advs.201903366.

13. Schwärzler, J., Mayr, L., Radlinger, B., Grabherr, F., Philipp, M., Texler, B., Grander, C., Ritsch, A., Hunjadi, M., Enrich, B., et al. (2022). Adipocyte GPX4 protects against inflammation, hepatic insulin resistance and metabolic dysregulation. Int. J. Obes. (Lond) *46*, 951–959. https://doi.org/10.1038/s41366-022-01064-9.

14. Doll, S., Freitas, F.P., Shah, R., Aldrovandi, M., da Silva, M.C., Ingold, I., Goya Grocin, A., Xavier da Silva, T.N., Panzilius, E., Scheel, C.H., et al. (2019). FSP1 is a glutathione-independent ferroptosis suppressor. Nature *575*, 693–698. https://doi.org/10.1038/s41586-019-1707-0.

15. Fang, X., Cai, Z., Wang, H., Han, D., Cheng, Q., Zhang, P., Gao, F., Yu, Y., Song, Z., Wu, Q., et al. (2020). Loss of cardiac ferritin H facilitates cardiomyopathy via Slc7a11-mediated ferroptosis. Circ. Res. *127*, 486–501. https://doi.org/10.1161/CIRCRESAHA.120.316509.

16. Joffin, N., Gliniak, C.M., Funcke, J.B., Paschoal, V.A., Crewe, C., Chen, S., Gordillo, R., Kusminski, C.M., Oh, D.Y., Geldenhuys, W.J., et al. (2022). Adipose tissue macrophages exert systemic metabolic control by manipulating local iron concentrations. Nat. Metab. *4*, 1474–1494. https://doi.org/10.1038/s42255-022-00664-z.

17. Petersen, M.C., Smith, G.I., Palacios, H.H., Farabi, S.S., Yoshino, M., Yoshino, J., Cho, K., Davila-Roman, V.G., Shankaran, M., Barve, R.A., et al. (2024). Cardiometabolic characteristics of people with metabolically healthy and unhealthy obesity. Cell Metab. *36*, 745–761.e5. https://doi.org/10.1016/j.cmet.2024.03.002.

18. Xu, Y., Liu, Y., Li, K., Yuan, D., Yang, S., Zhou, L., Zhao, Y., Miao, S., Lv, C., and Zhao, J. (2022). COX-2/PGE2 pathway inhibits the ferroptosis induced by cerebral ischemia reperfusion. Mol. Neurobiol. *59*, 1619–1631. https://doi.org/10.1007/s12035-021-02706-1.

19. Aleem, A.M., Kang, W., Lin, S., Milad, M., Kingsley, P.J., Crews, B.C., Uddin, M.J., Rouzer, C.A., and Marnett, L.J. (2023). Ferroptosis inhibitors suppress prostaglandin synthesis in lipopolysaccharide-stimulated macrophages. ACS Chem. Biol. *18*, 404–418. https://doi.org/10.1021/acschembio.2c00869.

20. Lee, J.Y., Nam, M., Son, H.Y., Hyun, K., Jang, S.Y., Kim, J.W., Kim, M.W., Jung, Y., Jang, E., Yoon, S.J., et al. (2020). Polyunsaturated fatty acid biosynthesis pathway determines ferroptosis sensitivity in gastric cancer. Proc. Natl. Acad. Sci. USA *117*, 32433–32442. https://doi.org/10.1073/pnas.2006828117.

21. Song, X., Liu, J., Kuang, F., Chen, X., Zeh, H.J., 3rd, Kang, R., Kroemer, G., Xie, Y., and Tang, D. (2021). PDK4 dictates metabolic resistance to ferroptosis by suppressing pyruvate oxidation and fatty acid synthesis. Cell Rep. *34*, 108767. https://doi.org/10.1016/j.celrep.2021.108767.

22. Panda, S.K., Peng, V., Sudan, R., Ulezko Antonova, A., Di Luccia, B., Ohara, T.E., Fachi, J.L., Grajales-Reyes, G.E., Jaeger, N., Trsan, T., et al. (2023). Repression of the aryl-hydrocarbon receptor prevents oxidative stress and ferroptosis of intestinal intraepithelial lymphocytes. Immunity *56*, 797–812.e4. https://doi.org/10.1016/j.immuni.2023.01.023.

23. Zuo, X., Zeng, H., Wang, B., Yang, X., He, D., Wang, L., Ouyang, H., and Yuan, J. (2022). AKR1C1 protects corneal epithelial cells against oxidative stress-mediated ferroptosis in dry eye. Invest. Ophthalmol. Vis. Sci. *63*, 3. https://doi.org/10.1167/iovs.63.10.3.

24. Park, M.W., Cha, H.W., Kim, J., Kim, J.H., Yang, H., Yoon, S., Boonpraman, N., Yi, S.S., Yoo, I.D., and Moon, J.S. (2021). NOX4 promotes ferroptosis of astrocytes by oxidative stress-induced lipid peroxidation via the impairment of mitochondrial metabolism in Alzheimer's diseases. Redox Biol. *41*, 101947. https://doi.org/10.1016/j.redox.2021.101947.

25. Zhu, K., Zhu, X., Liu, S., Yu, J., Wu, S., and Hei, M. (2022). Glycyrrhizin attenuates hypoxic-ischemic brain damage by inhibiting ferroptosis and neuroinflammation in neonatal rats via the HMGB1/GPX4 pathway. Oxid. Med. Cell. Longev. *2022*, 8438528. https://doi.org/10.1155/2022/8438528.

26. Zhu, K., Zhu, X., Sun, S., Yang, W., Liu, S., Tang, Z., Zhang, R., Li, J., Shen, T., and Hei, M.J.E.n. (2021). Inhibition of TLR4 prevents hippocampal hypoxic-ischemic injury by regulating ferroptosis in neonatal rats. Exp. Neurol. *345*, 113828. https://doi.org/10.1016/j.expneurol.2021.113828.

27. Tao, L., Yang, X., Ge, C., Zhang, P., He, W., Xu, X., Li, X., Chen, W., Yu, Y., Zhang, H., et al. (2024). Integrative clinical and preclinical studies identify FerroTerminator1 as a potent therapeutic drug for MASH. Cell Metab. *36*, 2190–2206.e5. https://doi.org/10.1016/j.cmet.2024.07.013.

28. Yang, M., Chen, P., Liu, J., Zhu, S., Kroemer, G., Klionsky, D.J., Lotze, M.T., Zeh, H.J., Kang, R., and Tang, D. (2019). Clockophagy is a novel selective autophagy process favoring ferroptosis. Sci. Adv. *5*, eaaw2238. https://doi.org/10.1126/sciadv.aaw2238.

29. Cho, S.S., Yang, J.H., Lee, J.H., Baek, J.S., Ku, S.K., Cho, I.J., Kim, K.M., and Ki, S.H. (2022). Ferroptosis contribute to hepatic stellate cell activation and liver fibrogenesis. Free Radic. Biol. Med. *193*, 620–637. https://doi.org/10.1016/j.freeradbiomed.2022.11.011.

30. Zhang, Y., Swanda, R.V., Nie, L., Liu, X., Wang, C., Lee, H., Lei, G., Mao, C., Koppula, P., Cheng, W., et al. (2021). mTORC1 couples cyst(e)ine availability with GPX4 protein synthesis and ferroptosis regulation. Nat. Commun. *12*, 1589. https://doi.org/10.1038/s41467-021-21841-w.

31. Yang, W.S., Kim, K.J., Gaschler, M.M., Patel, M., Shchepinov, M.S., and Stockwell, B.R. (2016). Peroxidation of polyunsaturated fatty acids by lipoxygenases drives ferroptosis. Proc. Natl. Acad. Sci. USA *113*, E4966–E4975. https://doi.org/10.1073/pnas.1603244113.

32. Zeng, W., Long, X., Liu, P.S., and Xie, X. (2023). The interplay of oncogenic signaling, oxidative stress and ferroptosis in cancer. Int. J. Cancer *153*, 918–931. https://doi.org/10.1002/ijc.34486.

33. Yuan, L.Q., Wang, C., Lu, D.F., Zhao, X.D., Tan, L.H., and Chen, X. (2020). Induction of apoptosis and ferroptosis by a tumor suppressing magnetic field through ROS-mediated DNA damage. Aging (Albany, NY) *12*, 3662–3681. https://doi.org/10.18632/aging.102836.

34. Shen, D., Luo, J., Chen, L., Ma, W., Mao, X., Zhang, Y., Zheng, J., Wang, Y., Wan, J., Wang, S., et al. (2022). PARPi treatment enhances radiotherapy-induced ferroptosis and antitumor immune responses via the cGAS signaling pathway in colorectal cancer. Cancer Lett. *550*, 215919. https://doi.org/10.1016/j.canlet.2022.215919.

35. Chen, P.H., Wu, J., Ding, C.C., Lin, C.C., Pan, S., Bossa, N., Xu, Y., Yang, W.H., Mathey-Prevot, B., and Chi, J.T. (2020). Kinome screen of ferroptosis reveals a novel role of ATM in regulating iron metabolism. Cell Death Differ. *27*, 1008–1022. https://doi.org/10.1038/s41418-019-0393-7.

36. Wong, B.W., Kuchnio, A., Bruning, U., and Carmeliet, P. (2013). Emerging novel functions of the oxygen-sensing prolyl hydroxylase domain enzymes. Trends Biochem. Sci. *38*, 3–11. https://doi.org/10.1016/j.tibs.2012.10.004.

37. Jiang, C., Qu, A., Matsubara, T., Chanturiya, T., Jou, W., Gavrilova, O., Shah, Y.M., and Gonzalez, F.J. (2011). Disruption of hypoxia-inducible factor 1 in adipocytes improves insulin sensitivity and decreases adiposity in high-fat diet-fed mice. Diabetes *60*, 2484–2495. https://doi.org/10.2337/db11-0174.

38. Zhao, G.N., Tian, Z.W., Tian, T., Zhu, Z.P., Zhao, W.J., Tian, H., Cheng, X., Hu, F.J., Hu, M.L., Tian, S., et al. (2021). TMBIM1 is an inhibitor of adipogenesis and its depletion promotes adipocyte hyperplasia and improves obesity-related metabolic disease. Cell Metab. *33*, 1640–1654.e8. https://doi.org/10.1016/j.cmet.2021.05.014.

39. Senol-Cosar, O., Flach, R.J.R., DiStefano, M., Chawla, A., Nicoloro, S., Straubhaar, J., Hardy, O.T., Noh, H.L., Kim, J.K., Wabitsch, M., et al. (2016). Tenomodulin promotes human adipocyte differentiation and beneficial visceral adipose tissue expansion. Nat. Commun. *7*, 10686. https://doi.org/10.1038/ncomms10686.

40. Wang, Y., Zhang, M., Bi, R., Su, Y., Quan, F., Lin, Y., Yue, C., Cui, X., Zhao, Q., Liu, S., et al. (2022). ACSL4 deficiency confers protection against ferroptosis-mediated acute kidney injury. Redox Biol. *51*, 102262. https://doi.org/10.1016/j.redox.2022.102262.

41. Li, Y., Feng, D., Wang, Z., Zhao, Y., Sun, R., Tian, D., Liu, D., Zhang, F., Ning, S., Yao, J., et al. (2019). Ischemia-induced ACSL4 activation contributes to ferroptosis-mediated tissue injury in intestinal ischemia/reperfusion. Cell Death Differ. *26*, 2284–2299. https://doi.org/10.1038/s41418-019-0299-4.

42. Wang, M.E., Chen, J., Lu, Y., Bawcom, A.R., Wu, J., Ou, J., Asara, J.M., Armstrong, A.J., Wang, Q., Li, L., et al. (2023). RB1-deficient prostate tumor growth and metastasis are vulnerable to ferroptosis induction via the E2F/ACSL4 axis. J. Clin. Invest. *133*, e166647. https://doi.org/10.1172/JCI166647.

43. He, S., Li, R., Peng, Y., Wang, Z., Huang, J., Meng, H., Min, J., Wang, F., and Ma, Q. (2022). ACSL4 contributes to ferroptosis-mediated rhabdomyolysis in exertional heat stroke. J. Cachexia Sarcopenia Muscle *13*, 1717–1730. https://doi.org/10.1002/jcsm.12953.

44. Bi, X., Wu, X., Chen, J., Li, X., Lin, Y., Yu, Y., Fang, X., Cheng, X., Cai, Z., Jin, T., et al. (2024). Characterization of ferroptosis-triggered pyroptotic signaling in heart failure. Signal Transduct. Target. Ther. *9*, 257. https://doi.org/10.1038/s41392-024-01962-6.

45. Ayala, A., Muñoz, M.F., and Argüelles, S. (2014). Lipid peroxidation: production, metabolism, and signaling mechanisms of malondialdehyde and 4-hydroxy-2-nonenal. Oxid. Med. Cell. Longev. *2014*, 360438. https://doi.org/10.1155/2014/360438.

46. Doll, S., Proneth, B., Tyurina, Y.Y., Panzilius, E., Kobayashi, S., Ingold, I., Irmler, M., Beckers, J., Aichler, M., Walch, A., et al. (2017). ACSL4 dictates ferroptosis sensitivity by shaping cellular lipid composition. Nat. Chem. Biol. *13*, 91–98. https://doi.org/10.1038/nchembio.2239.

47. Tejera, N., Boeglin, W.E., Suzuki, T., and Schneider, C. (2012). COX-2-dependent and -independent biosynthesis of dihydroxy-arachidonic acids in activated human leukocytes. J. Lipid Res. *53*, 87–94. https://doi.org/10.1194/jlr.M017822.

48. Belkaid, A., Ouellette, R.J., and Surette, M.E. (2017). 17beta-estradiol-induced ACSL4 protein expression promotes an invasive phenotype in estrogen receptor positive mammary carcinoma cells. Carcinogenesis *38*, 402–410. https://doi.org/10.1093/carcin/bgx020.

49. Dierge, E., Debock, E., Guilbaud, C., Corbet, C., Mignolet, E., Mignard, L., Bastien, E., Dessy, C., Larondelle, Y., and Feron, O. (2021). Peroxidation of n-3 and n-6 polyunsaturated fatty acids in the acidic tumor environment leads to ferroptosis-mediated anticancer effects. Cell Metab. *33*, 1701–1715.e5. https://doi.org/10.1016/j.cmet.2021.05.016.

50. Rui, T., Wang, H., Li, Q., Cheng, Y., Gao, Y., Fang, X., Ma, X., Chen, G., Gao, C., Gu, Z., et al. (2021). Deletion of ferritin H in neurons counteracts the protective effect of melatonin against traumatic brain injury-induced ferroptosis. J. Pineal Res. *70*, e12704. https://doi.org/10.1111/jpi.12704.

51. Vanoaica, L., Darshan, D., Richman, L., Schümann, K., and Kühn, L.C. (2010). Intestinal ferritin H is required for an accurate control of iron absorption. Cell Metab. *12*, 273–282. https://doi.org/10.1016/j.cmet.2010.08.003.

52. Darshan, D., Vanoaica, L., Richman, L., Beermann, F., and Kühn, L.C. (2009). Conditional deletion of ferritin H in mice induces loss of iron storage and liver damage. Hepatology *50*, 852–860. https://doi.org/10.1002/hep.23058.

53. Brestoff, J.R., Wilen, C.B., Moley, J.R., Li, Y., Zou, W., Malvin, N.P., Rowen, M.N., Saunders, B.T., Ma, H., Mack, M.R., et al. (2021). Intercellular mitochondria transfer to macrophages regulates white adipose tissue homeostasis and is impaired in obesity. Cell Metab. *33*, 270–282.e8. https://doi.org/10.1016/j.cmet.2020.11.008.

54. Blankenhaus, B., Braza, F., Martins, R., Bastos-Amador, P., González-García, I., Carlos, A.R., Mahu, I., Faisca, P., Nunes, J.M., Ventura, P., et al. (2019). Ferritin regulates organismal energy balance and thermogenesis. Mol. Metab. *24*, 64–79. https://doi.org/10.1016/j.molmet.2019.03.008.

55. Crane, J.D., Mottillo, E.P., Farncombe, T.H., Morrison, K.M., and Steinberg, G.R. (2014). A standardized infrared imaging technique that specifically detects UCP1-mediated thermogenesis in vivo. Mol. Metab. *3*, 490–494. https://doi.org/10.1016/j.molmet.2014.04.007.

56. Jin, L., Han, S., Lv, X., Li, X., Zhang, Z., Kuang, H., Chen, Z., Lv, C.A., Peng, W., Yang, Z., et al. (2023). The muscle-enriched myokine Musclin impairs beige fat thermogenesis and systemic energy homeostasis via Tfr1/PKA signaling in male mice. Nat. Commun. *14*, 4257. https://doi.org/10.1038/s41467-023-39710-z.

57. Chen, Y., Wu, Z., Huang, S., Wang, X., He, S., Liu, L., Hu, Y., Chen, L., Chen, P., Liu, S., et al. (2022). Adipocyte IRE1alpha promotes PGC1alpha mRNA decay and restrains adaptive thermogenesis. Nat. Metab. *4*, 1166–1184. https://doi.org/10.1038/s42255-022-00631-8.

58. Sonoda, J., Mehl, I.R., Chong, L.W., Nofsinger, R.R., and Evans, R.M. (2007). PGC-1beta controls mitochondrial metabolism to modulate circadian activity, adaptive thermogenesis, and hepatic steatosis. Proc. Natl. Acad. Sci. USA *104*, 5223–5228. https://doi.org/10.1073/pnas.0611623104.

59. Bean, C., Audano, M., Varanita, T., Favaretto, F., Medaglia, M., Gerdol, M., Pernas, L., Stasi, F., Giacomello, M., Herkenne, S., et al. (2021). The mitochondrial protein Opa1 promotes adipocyte browning that is dependent on urea cycle metabolites. Nat. Metab. *3*, 1633–1647. https://doi.org/10.1038/s42255-021-00497-2.

60. Uldry, M., Yang, W., St-Pierre, J., Lin, J., Seale, P., and Spiegelman, B.M. (2006). Complementary action of the PGC-1 coactivators in mitochondrial biogenesis and brown fat differentiation. Cell Metab. *3*, 333–341. https://doi.org/10.1016/j.cmet.2006.04.002.

61. Zhang, H., Gao, P., Fukuda, R., Kumar, G., Krishnamachary, B., Zeller, K.I., Dang, C.V., and Semenza, G.L. (2007). HIF-1 inhibits mitochondrial biogenesis and cellular respiration in VHL-deficient renal cell carcinoma by repression of C-MYC activity. Cancer Cell *11*, 407–420. https://doi.org/10.1016/j.ccr.2007.04.001.

62. Montanari, T., Pošćić, N., and Colitti, M. (2017). Factors involved in white-to-brown adipose tissue conversion and in thermogenesis: a review. Obes. Rev. *18*, 495–513. https://doi.org/10.1111/obr.12520.

63. Ceddia, R.P., Zurawski, Z., Thompson Gray, A., Adegboye, F., McDonald-Boyer, A., Shi, F., Liu, D., Maldonado, J., Feng, J., Li, Y., et al. (2023). Gbetagamma-SNAP25 exocytotic brake removal enhances insulin action, promotes adipocyte browning, and protects against diet-induced obesity. J. Clin. Invest. *133*, e160617. https://doi.org/10.1172/JCI160617.

64. Fain, J.N., Ballou, L.R., and Bahouth, S.W. (2001). Obesity is induced in mice heterozygous for cyclooxygenase-2. Prostaglandins Other Lipid Mediat. *65*, 199–209. https://doi.org/10.1016/s0090-6980(01)00136-8.

65. Vegiopoulos, A., Müller-Decker, K., Strzoda, D., Schmitt, I., Chichelnitskiy, E., Ostertag, A., Berriel Diaz, M., Rozman, J., Hrabe de Angelis, M., Nüsing, R.M., et al. (2010). Cyclooxygenase-2 controls energy homeostasis in mice by de novo recruitment of brown adipocytes. Science *328*, 1158–1161. https://doi.org/10.1126/science.1186034.

66. Xiao, L., De Jesus, D.F., Ju, C.W., Wei, J.B., Hu, J., DiStefano-Forti, A., Tsuji, T., Cero, C., Männistö, V., Manninen, S.M., et al. (2024). m(6)A mRNA methylation in brown fat regulates systemic insulin sensitivity via an inter-organ prostaglandin signaling axis independent of UCP1. Cell Metab. *36*, 2207–2227.e9. https://doi.org/10.1016/j.cmet.2024.08.006.

67. Han, Y.H., Buffolo, M., Pires, K.M., Pei, S., Scherer, P.E., and Boudina, S. (2016). Adipocyte-specific deletion of manganese superoxide dismutase protects from diet-induced obesity through increased mitochondrial uncoupling and biogenesis. Diabetes *65*, 2639–2651. https://doi.org/10.2337/db16-0283.

68. Iwasaki, T., Nakajima, A., Yoneda, M., Yamada, Y., Mukasa, K., Fujita, K., Fujisawa, N., Wada, K., and Terauchi, Y. (2005). Serum ferritin is associated with visceral fat area and subcutaneous fat area. Diabetes Care *28*, 2486–2491. https://doi.org/10.2337/diacare.28.10.2486.

69. Wrede, C.E., Buettner, R., Bollheimer, L.C., Schölmerich, J., Palitzsch, K.D., and Hellerbrand, C. (2006). Association between serum ferritin and the insulin resistance syndrome in a representative population. Eur. J. Endocrinol. *154*, 333–340. https://doi.org/10.1530/eje.1.02083.

70. Chavakis, T., Alexaki, V.I., and Ferrante, A.W., Jr. (2024). Author Correction: macrophage function in adipose tissue homeostasis and metabolic inflammation. Nat. Immunol. *25*, 576. https://doi.org/10.1038/s41590-023-01726-4.

71. Cipolletta, D., Feuerer, M., Li, A., Kamei, N., Lee, J., Shoelson, S.E., Benoist, C., and Mathis, D. (2012). PPAR-gamma is a major driver of the accumulation and phenotype of adipose tissue Treg cells. Nature *486*, 549–553. https://doi.org/10.1038/nature11132.

72. Lee, Y.S., Kim, J.W., Osborne, O., Oh, D.Y., Sasik, R., Schenk, S., Chen, A., Chung, H., Murphy, A., Watkins, S.M., et al. (2014). Increased adipocyte O2 consumption triggers HIF-1alpha, causing inflammation and insulin resistance in obesity. Cell *157*, 1339–1352. https://doi.org/10.1016/j.cell.2014.05.012.

73. Hosogai, N., Fukuhara, A., Oshima, K., Miyata, Y., Tanaka, S., Segawa, K., Furukawa, S., Tochino, Y., Komuro, R., Matsuda, M., et al. (2007). Adipose tissue hypoxia in obesity and its impact on adipocytokine dysregulation. Diabetes *56*, 901–911. https://doi.org/10.2337/db06-0911.

74. Imagawa, M., Tsuchiya, T., and Nishihara, T. (1999). Identification of inducible genes at the early stage of adipocyte differentiation of 3T3-L1 cells. Biochem. Biophys. Res. Commun. *254*, 299–305. https://doi.org/10.1006/bbrc.1998.9937.

75. Jun, J.C., Devera, R., Unnikrishnan, D., Shin, M.K., Bevans-Fonti, S., Yao, Q., Rathore, A., Younas, H., Halberg, N., Scherer, P.E., et al. (2017). Adipose HIF-1α causes obesity by suppressing brown adipose tissue thermogenesis. J. Mol. Med. (Berl.) *95*, 287–297. https://doi.org/10.1007/s00109-016-1480-6.

76. Huang, Z., Zhong, L., Lee, J.T.H., Zhang, J., Wu, D., Geng, L., Wang, Y., Wong, C.M., and Xu, A. (2017). The FGF21-CCL11 axis mediates beiging of white adipose tissues by coupling sympathetic nervous system to Type 2 immunity. Cell Metab. *26*, 493–508.e4. https://doi.org/10.1016/j.cmet.2017.08.003.

77. Mehran, A.E., Templeman, N.M., Brigidi, G.S., Lim, G.E., Chu, K.Y., Hu, X., Botezelli, J.D., Asadi, A., Hoffman, B.G., Kieffer, T.J., et al. (2012). Hyperinsulinemia drives diet-induced obesity independently of brain insulin production. Cell Metab. *16*, 723–737. https://doi.org/10.1016/j.cmet.2012.10.019.

78. Wang, F. (2023). Ferrology: a charming boundless iron-centric science. Sci. Sin.-Vitae *53*, 1331–1344. https://doi.org/10.1360/SSV-2023-0192.

79. Wu, T., Hu, E., Xu, S., Chen, M., Guo, P., Dai, Z., Feng, T., Zhou, L., Tang, W., Zhan, L., et al. (2021). clusterProfiler 4.0: A universal enrichment tool for interpreting omics data. Innovation (Camb) *2*, 100141. https://doi.org/10.1016/j.xinn.2021.100141.

80. Liberzon, A., Subramanian, A., Pinchback, R., Thorvaldsdóttir, H., Tamayo, P., and Mesirov, J.P. (2011). Molecular signatures database (MSigDB) 3.0. Bioinformatics *27*, 1739–1740. https://doi.org/10.1093/bioinformatics/btr260.

81. Zhou, N., Yuan, X., Du, Q., Zhang, Z., Shi, X., Bao, J., Ning, Y., and Peng, L. (2023). FerrDb V2: update of the manually curated database of ferroptosis regulators and ferroptosis-disease associations. Nucleic Acids Res. *51*, D571–D582. https://doi.org/10.1093/nar/gkac935.

82. Mina, A.I., LeClair, R.A., LeClair, K.B., Cohen, D.E., Lantier, L., and Banks, A.S. (2018). CalR: A web-based analysis tool for indirect calorimetry experiments. Cell Metab. *28*, 656–666.e1. https://doi.org/10.1016/j.cmet.2018.06.019.

83. Zhang, Z., Zhang, F., Guo, X., An, P., Tao, Y., and Wang, F. (2012). Ferroportin1 in hepatocytes and macrophages is required for the efficient mobilization of body iron stores in mice. Hepatology *56*, 961–971. https://doi.org/10.1002/hep.25746.

84. Wang, P., Luo, R., Zhang, M., Wang, Y., Song, T., Tao, T., Li, Z., Jin, L., Zheng, H., Chen, W., et al. (2020). A cross-talk between epithelium and endothelium mediates human alveolar-capillary injury during SARS-CoV-2 infection. Cell Death Dis. *11*, 1042. https://doi.org/10.1038/s41419-020-03252-9.

85. Chen, Y., Jiang, H., Zhan, Z., Lu, J., Gu, T., Yu, P., Liang, W., Zhang, X., Liu, S., Bi, H., et al. (2023). Restoration of lipid homeostasis between TG and PE by the LXRα-ATGL/EPT1 axis ameliorates hepatosteatosis. Cell Death Dis. *14*, 85. https://doi.org/10.1038/s41419-023-05613-6.

Please cite this article in press as: Wang et al., Adipocyte-derived ferroptotic signaling mitigates obesity, Cell Metabolism (2024), https://doi.org/10.1016/j.cmet.2024.11.010

STAR★METHODS

KEY RESOURCES TABLE

REAGENT or RESOURCE	SOURCE	IDENTIFIER
Antibodies		
ACSL4 (F-4)	Santa Cruz Biotechnology	Cat# sc-365230; RRID:AB_10843105
EPAS-1 (190b)	Santa Cruz Biotechnology	Cat# sc-13596; RRID:AB_627525
Anti-xCT antibody	Abcam	Cat# ab37185; RRID:AB_778944
Anti-HIF-1 alpha antibody [EPR16897]	Abcam	Cat# ab179483; RRID:AB_2732807
Anti-PGC1 alpha + beta antibody	Abcam	Cat# ab72230; RRID:AB_1640773
Anti-15 Lipoxygenase 1 antibody [EPR22138]	Abcam	Cat# ab244205; RRID:AB_2910599
Anti-Ferritin Light Chain antibody	Abcam	Cat# ab69090; RRID:AB_1523609
Anti-Ferritin Heavy Chain antibody	Abcam	Cat# ab65080; RRID:AB_10564857
Anti-UCP3 + UCP1 antibody [EPR19006]	Abcam	Cat# ab193470
Anti-4 Hydroxynonenal antibody	Abcam	Cat# ab46545; RRID:AB_722490
Anti-Malondialdehyde antibody [11E3]	Abcam	Cat# ab243066
Anti-F4/80 antibody [SP115]	Abcam	Cat# ab111101; RRID: AB_10859466
CoraLite®594-conjugated GPX4 Monoclonal antibody	Proteintec	Cat# CL594-67763; RRID:AB_2920180
Lamin A/C (4C11) Mouse mAb	Cell Signaling Technology	Cat# 4777; RRID:AB_10545756
c-Myc (E5Q6W) Rabbit mAb	Cell Signaling Technology	Cat# 18583; RRID:AB_2895543
PHD-2/Egln1 (D31E11) Rabbit mAb	Cell Signaling Technology	Cat# 4835; RRID:AB_10561316
NF-κB p65 (D14E12) XP® Rabbit mAb	Cell Signaling Technology	Cat# 8242; RRID:AB_10859369
Cleaved Caspase-3 (Asp175) (5A1E) Rabbit mAb	Cell Signaling Technology	Cat# 9664; RRID:AB_2070042
Caspase-3 (D3R6Y) Rabbit mAb	Cell Signaling Technology	Cat# 14220; RRID:AB_2798429
Akt (pan) (C67E7) Rabbit mAb	Cell Signaling Technology	Cat# 4691; RRID:AB_915783
Phospho-Akt (Ser473) Antibody	Cell Signaling Technology	Cat# 9271; RRID:AB_329825
GAPDH Rabbit pAb	ABclonal	Cat# AC001; RRID:AB_2619673
β-Tubulin Mouse mAb	ABclonal	Cat# AC021; RRID:AB_2773004
ALOX5 Rabbit mAb	ABclonal	Cat# A2877; RRID:AB_2863022
β-Actin Rabbit mAb (High Dilution)	ABclonal	Cat# AC026
Rabbit Anti-Mouse Uncoupling Protein 1 (UCP1) IgG	Alpha Diagnostics	Cat# UCP11-A
Brilliant Violet 650™ anti-mouse CD11c Antibody	BioLegend	Cat# 117339; RRID:AB_2562414
LIVE/DEAD™ Fixable Yellow Dead Cell Stain Kit *for 405 nm excitation**80 assays*	Invitrogen	Cat# L34967
FITC Anti-Mouse CD45R/B220 Antibody[RA3.3A 1/6.1]	Elabscience	Cat# E-AB-F1112C
Elab Fluor® Red 780 Anti-Mouse/Human CD11b Antibody[M1/70]	Elabscience	Cat# E-AB-F1081S
Brilliant Violet 605™ anti-mouse F4/80 Antibody	BioLegend	Cat# 123133; RRID:AB_2562305
PerCP/Cyanine5.5 Anti-Mouse Ly6G Antibody[1A8]	Elabscience	Cat# E-AB-F1108J
APC Anti-Mouse Ly6C Antibody[Monts 1]	Elabscience	Cat# E-AB-F1121E
PE/Cyanine7 Anti-Mouse CD206/MMR Antibody[C068C2]	Elabscience	Cat# E-AB-F1135H
PE anti-mouse CD9 Antibody	BioLegend	Cat# 124805; RRID:AB_1279327
FITC Anti-Mouse CD90 Antibody[M5/49.4.1]	Elabscience	Cat# E-AB-F1283C
FITC Anti-Mouse CD19 Antibody[1D3]	Elabscience	Cat# E-AB-F0986C
FITC Anti-Mouse CD161/NK1.1 Antibody[PK136]	Elabscience	Cat# E-AB-F0987C
FITC Anti-Mouse TCRβ Antibody[H57-597 (HB218)]	Elabscience	Cat# E-AB-F1123C
Bacterial and Virus Strains		
pSLenti-EF1-mCherry-CMV-MCS-3XFLAG-WPRE	This paper	N/A
pSLenti-EF1-mCherry-CMV-Hif1α-3XFLAG-WPRE	This paper	N/A

(*Continued on next page*)

Please cite this article in press as: Wang et al., Adipocyte-derived ferroptotic signaling mitigates obesity, Cell Metabolism (2024), https://doi.org/10.1016/j.cmet.2024.11.010

Continued

REAGENT or RESOURCE	SOURCE	IDENTIFIER
Chemicals, peptides, and recombinant proteins		
10058-F4	Selleck	Cat# S7153
Tyloxapol	Sigma-Aldrich	Cat# T8761
MG132	Selleckchem	Cat# S2619
Triton X-100	Sigma-Aldrich	Cat# X100
RSL3	Selleck	Cat# S8155
Erastin	Selleck	Cat# S7242
Ferrostatin-1	Selleck	Cat# S7243
5(S)15(S)-DiHETE	MedChemExpress	Cat# HY-113492
Tween 80	Selleck	Cat# S6702
BODIPY™ 581/591 C11	Invitrogen	Cat# D3861
TRIzol Reagent	ThermoFisher Scientific	Cat# 15596026
SuperScript II Reverse Transcriptase	Invitrogen	Cat# 18064014
SYBR GreenER qPCR SuperMix Universal	Invitrogen	Cat# 11762500
RIPA lysis buffer	Beyotime	Cat# P0013B
Collagenase II	Sigma-Aldrich	Cat# C6885
Dispase II	Sigma-Aldrich	Cat# D4693
Protease and phosphatase inhibitor cocktail for general use, 50X	Beyotime	Cat# P1046
Collagenase IV	SOLARBIO	Cat# C8160
Insulin (for injection)	Sigma-Aldrich	Cat# I0516
Glucose (for injection)	Sigma-Aldrich	Cat#G7528
Insulin (for cell differentiation)	Yeyuan	Cat# S12033
DNase I	Roche	Cat#10104159001
Red blood cell lysis buffer	BioLegend	Cat# 420301
3,3′,5-Triiodo-L-thyronine sodium salt	Sigma-Aldrich	Cat# T6397
Dexamethasone	Sigma-Aldrich	Cat# D4902
Isobutylmethylxanthine	Sigma-Aldrich	Cat# I7018
Indomethacin	Sigma-Aldrich	Cat# I7378
Rosiglitazone	Cayman Chemical via Biomol	Cat# 71740
DMEM/F12	Biosharp	Cat# BL305A
Fetal bovine serum	Gibco	Cat#10099-141C
Penicillin-Streptomycin	Beyotime	Cat#C0222
DMEM	Agilent	Cat#103575-100
Glucose (seahorse assay)	Agilent	Cat#103577-100
Pyruvate	Agilent	Cat#103015
Glutamine	Agilent	Cat#103579-100
CL316,243	MedChemExpress	Cat#HY-116771A
DAPI	Sigma-Aldrich	Cat#D9542
Critical commercial assays		
Triglyceride Assay kit	SOLARBIO	Cat# BC0625
SteadyPure rapid RNA extraction kit	Accurate Biology	Cat# AG21023
Lipid Peroxidation MDA Assay Kit	Beyotime	Cat# S0131S
GSH and GSSG Assay Kit	Beyotime	Cat# S0053
PrimeScript™ RT reagent Kit	TAKARA	Cat# RR037A
Cell Counting Kit-8	Beyotime	Cat# C0038
IL-1 beta Mouse Uncoated ELISA Kit	Invitrogen	Cat# 88-7013-22
TNF alpha Mouse Uncoated ELISA Kit	Invitrogen	Cat# 88-7324-22
Caspase 3 Activity Assay Kit	Beyotime	Cat# C1116
Seahorse XF Cell Mito Stress Test Kit	Agilent	Cat# 103015-100

(*Continued on next page*)

Please cite this article in press as: Wang et al., Adipocyte-derived ferroptotic signaling mitigates obesity, Cell Metabolism (2024), https://doi.org/10.1016/j.cmet.2024.11.010

Continued

REAGENT or RESOURCE	SOURCE	IDENTIFIER
Bicinchoninic Acid Protein Assay	Beyotime	Cat# P0011
Free Fatty Acids (NEFA/FFA) Colorimetric Assay Kit	Elabscience®	Cat# E-BC-K792-M
Minute™ Total Protein Extraction Kit for Adipose Tissues/Cultured Adipocytes	Invent Biotechnologies	Cat# AT-022
Minute Cytoplasmic and Nuclear Extraction Kit	Invent Biotechnologies	Cat# SC-003
Deposited Data		
Mendeley Data	https://data.mendeley.com/	https://data.mendeley.com/datasets/9h9b224k26/1
Raw data for graphs	This paper	Data S1
Experimental models: Organisms/strains		
C57BL6/J	Jackson Laboratories	JAX:000664
B6.129-*Fth1*$^{tm1.1Lck}$/J	Jackson Laboratories	JAX:018063
H11-e(CAG-LSL-Acsl4-IRES-tdTomato-Wpre-pA)1 mice	This paper	N/A
Hif1α$^{fl/fl}$ mice	Developed in the Xie Lab (Southern Medical University)	N/A
Adiponectin-Cre mice	Developed in the Xie Lab (Southern Medical University)	N/A
Oligonucleotides		
Primer sequences for genotyping, see Table S3	This paper	N/A
Primer sequences for quantitative RT-PCR, see Table S4	This paper	N/A
Software and algorithms		
GraphPad Software	GraphPad Prism	https://www.graphpad.com/scientific-software/prism/
ImageJ	NIH	https://ImageJ.nih.gov/ij/Vertion 9.0
FlowJo	FlowJo	https://www.flowjo.com/
Image Lab	Bio-Rad	https://www.biorad.com/en-us/product/image-lab-software?ID=KRE6P5E8Z

EXPERIMENTAL MODEL AND SUBJECT DETAILS

Human study

Association analysis between obesity and adipose ferroptosis

5,123 differentially expressed genes (DEGs) between individuals who are metabolically healthy and lean (MHL) and individuals with metabolically unhealthy obesity (MUO) were directly obtained from a previous study.[17] Briefly, individuals who were metabolically healthy and lean (MHL, n = 15) were defined as having a body mass index (BMI) of 18.5–24.9 kg/m^2, normal plasma triglycerides (< 150 mg/dL) and normal whole-body insulin sensitivity. Individuals with metabolically unhealthy obesity (MUO, n = 20) were defined as having a BMI of 30.0–49.9 kg/m^2, hepatic steatosis, and impaired whole-body insulin sensitivity.[17]

These DEGs were identified using $\log_2$-transformed counts per million (CPM) reads, applying a fold change cutoff of 1.25 and a nominal p-value < 0.05 with the limma package. Subsequently, functional annotation of the DEGs was performed using the clusterProfiler package, leveraging the enrichGO, enrichKEGG, enricher, enrichPathway, and enrichWP functions, based on Gene Ontology – Biological Process (GO-BP), Kyoto Encyclopedia of Genes and Genomes (KEGG), The Molecular Signatures Database (MsigDB), Reactome, and WikiPathways.[79,80] Additionally, 654 obesity-associated genes were retrieved from the curated Comparative Toxicogenomics Database (CTD) Gene-Disease Associations dataset[80] and 564 ferroptosis-related genes, classified into drivers, markers, suppressors, and unclassified, were sourced from FerrDBv2.[81] We examined the intersections among these three sets of genes to identify shared genes and elucidate potential biological pathways.

Human adipose analysis

Human biological samples, including abdominal adipose tissue and plasma samples (from a total of 20 donors; 10 male and 10 female; data shown in Table S2), were analyzed in this study. According to the BMI criteria by the Working Group on Obesity in China (WGOC), human samples were divided into control (BMI < 24), and obesity (BMI ≥ 28) groups. Sex was comparable between groups, as shown in Table S2. Adipose tissue samples were obtained from obese patients undergoing bariatric surgery, and lean patients

undergoing gastrointestinal surgery from the Zhongshan Hospital. The study protocol was approved by the Clinical Research Ethics Committee of Zhongshan Hospital of Fudan University with the approval number B2021-157R. All patients gave written consent for their samples to be collected.

Mouse models

*F*th-floxed (*Fth*$^{fl/fl}$) mice were purchased from the Jackson Laboratory (stock numbers 018063). *Hif1α*-floxed (*Hif1α*$^{fl/fl}$) mice and *Adiponectin-Cre* mice were kindly provided by Dr. Liwei Xie (Zhujiang Hospital Southern Medical University).[12] Conditional *Acsl4* transgenic mice were generated by Shanghai Model Organisms Center. In brief, a Rosa26 locus–targeting vector was used in which CAG promoter-driven expression of both the transgene and the fluorescent protein tdTomato is prevented by a LoxP-flanked STOP cassette; the transgenic mice express the *Acsl4* transgene and tdTomato upon Cre-mediated excision of the STOP cassette. All mouse lines were maintained on the C57BL/6 background, and mice were genotyped by performing PCR on genomic DNA obtained via tail biopsy, using the primers listed in Table S3. All animal studies were approved by the Institutional Animal Care and Use Committee at Zhejiang University and were conducted in accordance with the National Institutes of Health guidelines for animal care (No. ZJU20240536), and all animals were randomly assigned to cohorts when used. Except where indicated otherwise, adult (3-6 months of age) mice were used for the experiments, and all mice were housed in plastic cages at room temperature (22-24 degree) a 12 h/12 h light-dark cycle. The mice were supplied *ad libitum* with distilled water and either pelleted AIN-76A (Research Diets, New Brunswick, NJ) normal chow diet (NCD) containing a standard fat content (12% kcal derived from fat) or a high-fat diet (HFD) (cat. D12492, Research Diets) containing 60% kcal derived from fat. Male mice were used in the studies.

Cell culture

Adipose depots were surgically removed from 8-10-week-old wild-type mice and processed for SVF enrichment. In brief, the adipose tissues were manually minced and digested with 1.5 mg/mL collagenase II and 2.4 mg/mL dispase II in PBS containing 10% $CaCl_2$ (100 mM) for 45 min at 37°C with agitation. Digestion was quenched with DMEM/F12 medium containing 10% FBS, and the dissociated cells were passed through a 70-μm filter and then centrifuged at 400 × *g* for 5 min. The supernatant was discarded, and the SVF-containing pellet was resuspended in red blood cell lysis buffer for 5 min at room temperature and then quenched in DMEM/F12 containing 10% FBS. The cells were then passed through a 40-μm filter and collected by centrifugation at 400 × *g* for 5 min.

To differentiate SVFs isolated from iWAT into adipocytes, the cells were cultured in DMEM/F12 containing 10% FBS, 100 U/mL penicillin, 100 μg/mL Streptomycin, and full adipogenic cocktail containing 20 nM insulin, 1 nM T3, 1 μM dexamethasone, 0.5 mM isobutylmethylxanthine, and 125 nM indomethacin. To differentiate SVFs isolated from BAT into adipocytes, full adipogenic cocktail containing 20 nM insulin, 1 nM T3, 1 μM dexamethasone, 0.5 mM isobutylmethylxanthine,125 nM indomethacin and 2μM rosiglitazone. After 2 days the cells were transferred to adipogenic maintenance medium containing 20 nM insulin and 1 nM T3. The medium was changed every 2 days, and the cells were used for experiments within 7 days of the induction of differentiation.

METHOD DETAILS

Metabolic study

At 8 weeks of age, male mice were fed the NCD or HFD for at least 12 weeks. Serum total triglyceride (TG), total cholesterol (TC), low-density lipoprotein cholesterol (LDL-c), high-density lipoprotein cholesterol (LDL-c), alanine aminotransferase (ALT), aspartate aminotransferase (AST), lactate dehydrogenase (LDH), albumin (ALB), total protein (TP), creatine kinase (CK), blood urea nitrogen (BUN), and creatinine (CR) were measured using a biochemical analyzer. Non-esterified fatty acid (NEFA) levels were measured using a kit in accordance with the manufacturer's instructions. White blood cells (WBC), red blood cells (RBC), hemoglobin (HGB), mean corpuscular volume (MCV), platelets, platelets, neutrophils, lymphocytes, eosinophils, monocytes and basophils were analyzed by an auto hematology analyzer. For the glucose tolerance test, the mice were fasted overnight and then given an i.p. injection of glucose (1 g /kg body weight). For the insulin tolerance test, the mice were fasted for 4 h and then given an i.p. injection of insulin (0.5 units/kg body weight). To measure blood glucose concentration, whole blood was drawn from the tail vein at the indicated times, and blood glucose was measured using an AccuCheck glucometer (Roche, Indianapolis, IN). Oxygen consumption and energy expenditure was measured using indirect calorimetry with TSE PhenoMaster metabolic cages and calculated by *CalR*.[82] In brief, HFD-fed mice were placed in the metabolic cage at 10-11 weeks of age and allowed to acclimatize for 3 days prior to data analysis.

Seahorse assay

Oxygen consumption rate (OCRs) was determined using a Seahorse XFe96 analyzer (Agilent Technology). Specifically, Seahorse XF Cell Mito Stress Test Kit was employed according to instructions from the manufacturer. SVF cells were seeded on Seahorse XF96 plates and were differentiated into adipocytes following the procedures in **Cell culture**. Prior to assay, mature adipocytes (day 7 after differentiation) were changed as XF DMEM medium supplemented with 10 mM glucose, 1 mM pyruvate, 2 mM glutamine and incubated in a non-CO_2 incubator (37°C, 45 min). Cell plate was then placed in the analyzer following a preset mitochondria stress program with inhibitors injected as: Oligomycin (1.5 μM), FCCP (1.5 μM); Antimycin A/Rotenone (0.5μM) and respective measurements. OCRs were recorded and the ATP production, maximal respiration, and the spare respiratory capacity-dependent OCRs were calculated. Cell viability was also quantified using the CCK8 kit for normalization.

Please cite this article in press as: Wang et al., Adipocyte-derived ferroptotic signaling mitigates obesity, Cell Metabolism (2024), https://doi.org/10.1016/j.cmet.2024.11.010

Cold exposure assay

For cold exposure assays, mice were singly housed in pre-chilled cages without bedding in a cold chamber set at 4 °C or 6°C as indicated. Mice were granted free access to pre-chilled food and water during the whole assay. Core body temperature was monitored at indicated time points using a portable intelligent digital thermometer.

Infrared imaging

Body surface temperature was measured using a thermal imaging camera (FLOTRIC Camera). Mice were anesthetized with isoflurane and quietly laid on a whiteboard with their back up, followed by image capturing with the camera anchored at the same height for all mice in the same batch.

Topical cream application

RSL3-containing cream contained 5 mg RSL3 dissolved in 100 μL DMSO and then mixed with 215 mL lanolin, while the vehicle-containing control cream contained 100 μL DMSO mixed with 215 mL lanolin. Starting at 8 weeks of age, male mice were fed the HFD for 12 weeks; where applicable, 150 μL of cream was applied daily to the skin above the iWAT on both sides for the last 4 weeks on the HFD.

Lipid peroxidation measurement

Lipid peroxidation in primary cultured adipocytes was measured using confocal laser microscopy. In brief, SVFs were seeded on 24-well plates and incubated overnight. The next day, the cells were induced to differentiate into adipocytes as described above and treated with the indicated compounds for 7 days. The cells were then incubated in 200 μL PBS containing 5 μM C11-BODIPY 581/591 for 30 min at 37°C. Lipid ROS were then measured using confocal laser scanning microscopy with a 488-nm laser. For 4-HNE immunostaining, differentiated adipocytes were fixed in 4% paraformaldehyde in PBS for 20 min, then incubated in anti-4-HNE antibody in 3% BSA overnight, followed by incubated in goat anti-rabbit IgG conjugated with Alexa Fluor 594 antibody at 37°C for 1 h. Images were captured using a BX43 confocal microscope (Olympus) at 40× magnification. In addition, MDA content in cells and tissues were measured using the Lipid Peroxidation MDA Assay Kit in accordance with the manufacturer's protocol.

Glutathione measurement

SVFs were seeded into 6-well dishes. After 48 h, the cells were induced to differentiate into adipocytes as described above and treated with the indicated compounds for 7 days. The cells were then collected by scraping, and glutathione levels were measured using a Glutathione Assay Kit in accordance with the manufacturer's protocol. GSH and GSSG concentrations were calculated using a standard curve and normalized to total protein levels. For tissues, these concentrations were then normalized to tissue weight.

Tissue non-heme iron assay

Tissue non-heme iron was measured using the standard chromogen method as described previously.[83] In brief, homogenized tissues were incubated in NHI acid solution (10% trichloroacetic acid in 3 M HCl) at 65°C for 72 h. After centrifugation to pellet the debris, 10 μL supernatant was loaded into each well in a 96-well plate; 200 μL working solution containing 0.2% thioglycolic acid and 0.02% disodium 4,7-diphenyl-1,10-phenanthroline disulfonate in 50% saturated NaAc solution was added to each well, mixed, and the plate was incubated at room temperature for 10 min, after which absorbance was read at 535 nm using a spectrophotometer plate reader (Thermo Fisher). Iron concentration was normalized to the fresh tissue weight.

Histology and immunohistochemistry

Tissues were fixed overnight in 4% paraformaldehyde (pH 7.4), embedded in paraffin, and then serially sectioned. The sections were stained with hematoxylin and eosin (H&E) for routine histological examination with a light microscope. To measure cell death and ferroptosis in adipose tissues, select sections were stained with TUNEL, MDA, F4/80 and 4-HNE antibodies, respectively. Photomicrographs were obtained using an Eclipse E400 microscope (Nikon). For each mouse, three adjacent sections were quantified using ImageJ software.

Immunofluorescence staining

Cells were fixed in 4% paraformaldehyde for 20 min, washed three times in PBS, and then permeabilized with PBS containing 0.3% Triton X-100. After blocking with PBS containing 3% BSA, the cells were incubated in primary antibodies against HIF1α or HIF2α at 4°C overnight, washed three times in PBS, and then incubated in goat anti-rabbit IgG or goat anti-mouse IgG conjugated with Alexa Fluor 594 at 37°C for 1 h. After three washes in PBS, the nuclei were counterstained with DAPI. The cells were imaged at 40× magnification using a BX43 confocal microscope (Olympus).

Cell viability assay

SVFs were seeded in replicates of 6 onto 96-well plates at a density of 5000 per well. After 24 h, the cells were induced to differentiate into adipocytes as described above and treated with RSL3 and/or Fer-1 for 2, or 7 days. Subsequently, the medium was replaced with 100 μL fresh medium containing 10 μL Cell Counting Kit-8 reagent. After incubation for 1 h at 37°C in humidified air containing 5%

Please cite this article in press as: Wang et al., Adipocyte-derived ferroptotic signaling mitigates obesity, Cell Metabolism (2024), https://doi.org/10.1016/j.cmet.2024.11.010

CO_2, absorbance was measured at 450 nm, and cell viability was calculated in accordance with the manufacturer's instructions. For EC50 assay, SVFs were not induced to differentiate into adipocytes.

Oil Red O assay

Differentiated adipocytes prepared as described above were fixed in 10% formalin, rinsed in deionized water, and then incubated in 60% isopropanol for 5 min. The cells were then stained with Oil Red O working solution containing 2 g/L Oil Red O, 60% isopropanol, and 40% H_2O for 10 min at room temperature, washed five times in deionized water, incubated in isopropanol, and absorbance was measured at 500 nm.

Quantitative PCR

Total RNA was extracted using TRIzol reagent and cDNA was synthesized using SuperScript II Reverse Transcriptase. qRT–PCR was performed using SYBR GreenER qPCR SuperMix Universal, and triplicate samples were run on a Stratagene MX3000P qPCR system (Roche) in accordance with the manufacturer's protocol. The threshold cycle (Ct) values for each gene were normalized to *Rplp0*, and the $2^{-\Delta\Delta Ct}$ method was used for quantitative analysis. The primer sequences are listed in Table S4.

Western blot analysis

Nuclear and cytoplasmic fractions were prepared for western blot analysis using the Minute Cytoplasmic and Nuclear Extraction Kit in accordance with the manufacturer's instructions. Adipose tissues were lysed using the Minute™ Total Protein Extraction Kit for Adipose Tissues/Cultured Adipocytes in accordance with the manufacturer's instructions. Liver and muscle tissues were lysed using RIPA lysis buffer supplemented with protease and phosphatase inhibitor cocktail. After centrifugation, the supernatant was collected, and the protein concentration was measured using a Bicinchoninic Acid Protein Assay with a FLUOstar Omega microplate reader (BMG Labtech). The supernatant was mixed with 6× SDS loading buffer, and the samples were boiled for 10 min. Proteins were then loaded, separated using SDS-PAGE, and blotted using the appropriate antibodies. Anti Ucp3+Ucp1 and anti-Ucp1 were used for detection of thermogenesis in cultured adipocytes and adipose tissues, respectively. Most primary antibodies used for detection were diluted as 1:500 in 5% bovine serum albumin, 1XTBST, except for Gapdh, β-Tubulin and β-Actin, which were diluted as 1:10000. Secondary antibodies (Goat anti Rabbit IgG HRP or Goat anti Mouse IgG HRP) were diluted as 1:4000 in 5% slim milk, 1XTBST.

ELISAs

Mouse serum inflammation index including IL-1β and TNF-α were quantified by ELISA kits according to the manufacturer's instructions.

VLDL secretion assay

Mice were fasted for 16 hours and injected i.v. with tyloxapol (Sigma, T8761) at the dose of 500 mg/kg body weight. Blood samples were collected at indicated time points and the plasma was separated by centrifugation. Triglyceride measurements were performed in accordance with the manufacturer's instructions.

Caspase 3 activity

Adipose Caspase 3 activity was detected according to the manufacturer's instructions.

Lentivirus transduction

Lentivirus was produced by transfecting HEK293T cells with packaging plasmids (psPAX2), envelope plasmids (pMD2.G) and pSLenti-EF1-mCherry-CMV-MCS-3XFLAG-WPRE or pSLenti-EF1-mCherry-CMV-Hif1α-3XFLAG-WPRE in OBIO Tech. Inc. Lentivirus was mixed with Polybrene-plus (1μg/ml, OBIO), and then added into SVF cells (MOI of virus:cell=40:1 unless specifically described) cultured in DMEM/F12 supplemented with 10% FBS and 1%PS. After 20 hours, cells were changed with DMEM/F12 supplemented with 10% FBS and 1%PS for further use.

Tissue leukocyte isolation

SVFs containing leukocytes were isolated eWAT and iWAT following isolation of SVFs from mouse adipose tissue and were then stained and analyzed using flow cytometry. Spleens were finely minced in complete DMEM media containing 10% FBS and then digested with 1 mg/mL collagenase IV and 100 μg/mL DNase I for 35 min at 37°C while shaking at 180 rpm. EDTA-Na_2 was added to stop the digestion, and the cell suspension was passed through a 70-μm cell strainer (Corning), red blood cells were lysed using red blood cell lysis buffer, and splenocytes were pelleted and resuspended in FACS Buffer. The cells were then stained and analyzed using flow cytometry.

Flow cytometry

Leukocytes isolated from tissues were incubated with Fc block and LIVE/DEAD Fixable Yellow Dead Cell Stain Kit (1:1000) in 1× PBS at room temperature for 10 min, followed by sequential incubations with the corresponding fluorochrome-conjugated antibodies for 20 min at 4°C. The cells were then washed in 1× PBS containing 2% FBS, centrifuged at 350 × *g* for 4 min at 4°C, and resuspended in

Please cite this article in press as: Wang et al., Adipocyte-derived ferroptotic signaling mitigates obesity, Cell Metabolism (2024), https://doi.org/10.1016/j.cmet.2024.11.010

FACS Buffer for flow cytometry analysis using a an LSRFortessa X-20 cell analyser (BD Biosciences). The data were analyzed using FlowJo software V10, and macrophages were identified by excluding lineage markers (TCRβ, CD19, Nk1.1, and Ly6G) and the expression of CD11b, F4/80, CD11c, CD206, and CD9 using the gating strategy depicted in Figure S7B.

Proteomics LC–MS/MS and data analysis

Proteomics analysis was performed as previously described.[84] For enrichment of pathway analysis, the Kyoto Encyclopedia of Genes and Genomes (KEGG) database was used to identify enriched pathways using a two-tailed Fisher's exact test to test the enrichment of differentially expressed proteins against all identified proteins. Pathways with a corrected p-value <0.05 were considered significant. These pathways were classified into hierarchical categories using the KEGG website. For enrichment of protein domain analysis, for each category of proteins the InterPro database (a resource that provides functional analysis of protein sequences by classifying them into families and predicting the presence of domains and important sites) was searched, and a two-tailed Fisher's exact test was used to test enrichment of the differentially expressed proteins against all identified proteins. Protein domains with a corrected p-value <0.05 were considered significant.

Oxylipins analysis

Oxylipins were analyzed as previously described.[27] Significantly regulated metabolites between groups were determined by VIP and absolute $Log_2$2FC (fold change). VIP values were extracted from OPLS-DA result, which also contain score plots and permutation plots, was generated using R package MetaboAnalystR. The data was mean centering before OPLS-DA. In order to avoid overfitting, a permutation test (200 permutations) was performed.

Lipidomics analysis

Lipid metabolite profiling was carried out using a targeted quantitative lipidomics by Wuhan Metware Biotechnology Co., Ltd. (Wuhan, China), as previously described.[85] Differential metabolites were determined by VIP (VIP > 1) and P-value (P-value < 0.05, Student's t test). VIP values were extracted from OPLS-DA result, which also contain score plots and permutation plots, was generated using R package MetaboAnalystR. The data was log transform (log_2) and mean centering before OPLS-DA. In order to avoid overfitting, a permutation test (200 permutations) was performed.

QUANTIFICATION AND STATISTICAL ANALYSIS

Except where indicated otherwise, summary data are presented as the mean ± standard deviation or standard error of the mean. All analyses (except the proteomics analysis, lipidomics analysis and olylipins analysis; see above for details) were performed using Prism software v6 (GraphPad). Comparisons between two groups were analyzed using an unpaired Student's t-test; comparisons involving three or more related groups were analyzed using a one-way or two-way ANOVA with Sidak's multiple comparisons test. Quantifications of immunoblotting and IHC positive area were conducted by ImageJ. Experiments involving measurements of body weights, blood parameters, body surface temperature, core temperature, indirect calorimetry of mice were performed in a blinded fashion, with randomly-grouped mice based on their ear tag identification numbers. Imaging and histology were also performed and analyzed in a blinded fashion, prior to the decoding of the sample identities. No data points were excluded from the study expect for sample missing. The data were assumed to be continuous normal distribution.